

# Global Surface Winds and Aeolian Sediment Pathways on Mars from the Morphology of Barchan Dunes

Lior Rubanenko<sup>1</sup>, Andrew Gunn<sup>2</sup>, Sebastian Pérez-López<sup>3</sup>, Lori K Fenton<sup>4</sup>, Ryan C. Ewing<sup>5</sup>, Alejandro Soto<sup>6</sup>, and Mathieu G. A. Lapôtre<sup>3</sup>

<sup>1</sup>Stanford University

<sup>2</sup>University of Pennsylvania

<sup>3</sup>Stanford University

<sup>4</sup>SETI Institute

<sup>5</sup>Texas A&M University

<sup>6</sup>Southwest Research Institute

December 22, 2022

## Abstract

In the absence of consistent meteorological data on Mars, the morphology of dunes can be employed to study its atmosphere. Specifically, barchan dunes, which form under approximately unimodal winds, are reliable proxies for the dominant wind direction. Here, we characterize near-surface winds on Mars from the morphology of >106 barchans mapped globally on the planet by a convolutional neural network. Barchan migration is predominantly aligned with the global circulation: northerly at mid-latitudes and cyclonic near the north pole, with the addition of an anti-cyclonic north-polar component that likely originates from winds emerging from the ice cap. Locally, migration directions deviate from regional trends in areas with high topographic roughness. Notably, obstacles <100 km such as impact craters are efficient at deflecting surface winds. Our database, which provides insights into planetary-scale aeolian processes on modern-day Mars, can be used to constrain global circulation models to assist with predictions for future missions.

## **Global Surface Winds and Aeolian Sediment Pathways on Mars from the Morphology of Barchan Dunes**

**L. Rubanenko<sup>1,2</sup>, A. Gunn<sup>1,3</sup>, S. Pérez-López<sup>1</sup>, L.K. Fenton<sup>4</sup>, R.C. Ewing<sup>5</sup>, A. Soto<sup>6</sup> and M.G.A Lapôtre<sup>1</sup>**

<sup>1</sup> Department of Earth & Planetary Sciences, Stanford University, Stanford, California, USA.

<sup>2</sup> Civil and Environmental Engineering, Technion, Haifa, Israel.

<sup>3</sup> School of Earth, Atmosphere & Environment, Monash University, Clayton, Australia.

<sup>4</sup> Carl Sagan Center, SETI Institute, Mountain View, California, USA.

<sup>5</sup> Department of Geology & Geophysics, Texas A&M, College Station, Texas, USA.

<sup>6</sup> Southwest research Institute, Boulder, Colorado, USA.

Corresponding author: Lior Rubanenko ([liorr@stanford.edu](mailto:liorr@stanford.edu))

### **Key Points:**

- We derive global barchan dune migration directions on Mars using a convolutional neural network
- Aeolian sediment pathways on Mars are largely controlled by the planet's global circulation
- Surface winds are locally deflected by topographic obstacles < 100 km horizontal scales.

## Abstract

In the absence of consistent meteorological data on Mars, the morphology of dunes can be employed to study its atmosphere. Specifically, barchan dunes, which form under approximately unimodal winds, are reliable proxies for the dominant wind direction. Here, we characterize near-surface winds on Mars from the morphology of  $>10^6$  barchans mapped globally on the planet by a convolutional neural network. Barchan migration is predominantly aligned with the global circulation – northerly at mid-latitudes and cyclonic near the north pole – with the addition of an anti-cyclonic north-polar component that likely originates from winds emerging from the ice cap. Locally, migration directions deviate from regional trends in areas with high topographic roughness. Notably, obstacles  $<100$  km such as impact craters are efficient at deflecting surface winds. Our database, which provides insights into planetary-scale aeolian processes on modern-day Mars, can be used to constrain global circulation models to assist with predictions for future missions.

## Plain Language Summary

Crescent-shaped sand dunes are prevalent across the deserts of Mars. Here, we use the physical relationship between the shape of these dunes and the winds that form them to infer the directions of surface winds on Mars on a global scale. We find that dunes typically adhere to the global circulation patterns of Mars' atmosphere, and that local topographic winds are mostly important in areas with high topographic roughness such as inside deep impact craters. Our global wind map can serve to calibrate numerical climate models, which in turn can help us learn about the recent and modern-day climate of Mars.

## 1 Introduction

Winds have been a dominant driver of geologic activity on Mars, setting the pace of landscape erosion (Chojnacki et al., 2019), sediment transport and deposition (Baker et al., 2018; Bridges et al., 2012; Gunn et al., 2022), and controlling dust lifting (Greeley et al., 1981; Newman et al., 2004). Understanding the global circulation of modern surface winds is therefore not only important to model present-day atmospheric phenomena such as global dust storms in preparation for future crewed mission (e.g., Cantor et al., 2001; Greeley et al., 1981; Levine et al., 2018; Montabone & Forget, 2018), but also to calibrate global climate models (GCMs) that could then be used to decipher the planet's climatic record (Banham et al., 2018, 2021; Day & Dorn, 2019; Ewing et al., 2017; Fenton et al., 2005; Fenton & Hayward, 2010; Hayward et al., 2007; Kite, 2019; Lapôtre et al., 2020, 2021; Rubin et al., 2022; Tsoar et al., 1979; Ward et al., 1985; Wordsworth, 2016).

Crescentic (or barchan) dunes, which form under roughly unimodal winds in regions of limited sand supply, are widespread across the modern arid landscapes of Mars (Breed et al., 1979; Diniega et al., 2021; Fenton, 2020; Hayward et al., 2007, 2012; Rubanenko et al., 2021). The morphology of actively migrating barchan dunes can be used to infer the dominant wind direction and aeolian sediment transport pathways. The crestline orientation near the slipface center and horn orientations of actively migrating barchan dunes indicate the dominant wind and sediment transport directions (Figure 1; e.g., Gao et al., 2015). In some cases, the horns can become asymmetric, e.g., in the presence of a secondary wind component, as a result of dune-dune interactions, or topography (Bourke & Goudie, 2009; Parteli et al., 2014; Tsoar & Parteli, 2016). Thus, orbiter observations of barchan dunes have been used to indirectly characterize surface winds on Mars, where meteorological data is scarce (Hayward et al., 2007, 2012; Tsoar et al.,

1979). However, the majority of investigations that mapped individual dune migration directions focused on local-regional phenomena, as examining individual dunes globally has remained challenging (Ward et al., 1985). In contrast, the global database of Hayward et al. (2012) reports average slipface azimuths from  $\sim 10,000$  measurements,  $\sim 25\%$  of which were barchans.

Here, we expand the database of mapped barchan dunes by using higher resolution Mars Reconnaissance Orbiter Context Camera images (MRO CTX, Malin et al., 2007) as well as including recently mapped smaller dune fields (Fenton, 2020), which allows us to include barchan dunes in non-polar latitudes. We analyze a global dataset of barchan-dune outlines previously mapped on Mars by a convolutional neural network (Rubanenko et al., 2021). From dune outlines, we infer the orientation of dune slip-faces and horns (and their asymmetry) to infer local and global barchan migration patterns, driven by Mars' dominant near-surface winds and aeolian sediment transport pathways on a planetary scale. We further quantify the influence of topography on local winds by analyzing horn asymmetry and deviations between local dune migration direction and modeled regional winds. Altogether, our results provide a new global view of wind-driven sand transport on modern Mars that could be used to benchmark and refine GCM simulations of Mars' winds.

## 2 Methods

### 2.1 Automatic Measurement of Dune-Migration Direction

A convolutional neural network (CNN) is a type of machine learning technique that excels at tasks that require abstraction, such as object detection and segmentation in images. The CNN we employ in this study, Mask R-CNN (He et al., 2017), outlines objects in images by generalizing from a manually labeled dataset through an optimization process called *training*. Here, we employ a dataset of barchan dunes' outlines compiled by Rubanenko et al. (2021), who trained Mask R-CNN on images of barchan dunes tiled from the global MRO CTX mosaic (5 m/px) of Dickson et al. (2018). The trained model, which achieved a detection mean average precision of 77%, was used to automatically outline barchan dunes across the surface of Mars.

To spare computation time, and since the goal was to characterize known dunes and not to detect new ones, Rubanenko et al. (2021) focused on regions that were found to contain dune fields in previous investigations (Fenton, 2020; Hayward et al., 2007) between latitudes  $-70^{\circ}\text{N}$  and  $70^{\circ}\text{N}$ . Poleward of  $\pm 70^{\circ}\text{N}$ , all CTX images were inspected for the presence of barchan dunes. Through this process, the CNN detected over a million individual isolated barchan dunes on Mars, which were subsequently filtered to increase the robustness of the results (Rubanenko et al., 2022; Supplementary Materials). After manually reviewing a representative sample of the model detections, Rubanenko et al. (2022) elected to ignore any detections poleward of  $-70^{\circ}\text{N}$  due to the presence of sublimation-related features, such as spiders (Zuber, 2003), which the model occasionally misclassified as barchan dunes.

To measure the migration direction of a single barchan dune, we follow the procedure developed in Rubanenko et al. (2022). The algorithm automatically identifies six reference points

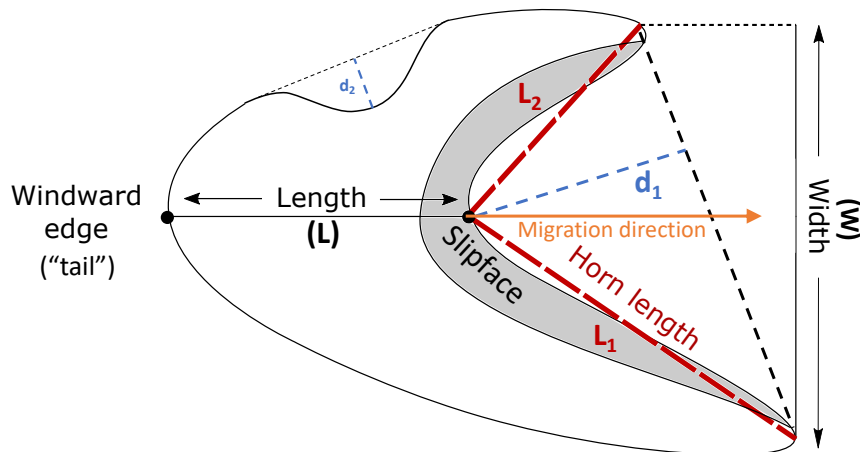


Figure 1: Definition of morphometric parameters. The dune slipface is identified as the deepest convexity defect along the dune contour (e.g.,  $d_1 > d_2$ ), and horns lengths ( $L_1$  and  $L_2$ ) are measured as the distance between the slipface and the horn apices.

along the dune contour: the center of the slipface, the two horn apices, the “tail” (upwind edge of the stoss) and sides. For relatively symmetric dunes (arbitrarily defined here as horn length ratio  $\max(L_1, L_2)/\min(L_1, L_2) < 2$ ), the migration direction is estimated as the bisector vector to the angle formed by the slipface center and horn apices (e.g., green arrows in Figure 2c–g). For asymmetric dunes ( $\max(L_1, L_2)/\min(L_1, L_2) > 2$ ), the migration direction was approximated to be in the direction of the line that links the tail to the slipface center (e.g., orange arrows in Figure 2c–g). To improve the robustness of our results, we further removed dunes with convexity defects  $< 2.5\%$  the dune length ( $L$  in Figure 1), and dunes for which the ratio between the second-deepest and deepest convexity defects ( $d_2/d_1$  Figure 1) exceeds 10%. The latter condition removed dunes with noisy contours, either due to mis-segmentation by the model or from natural complexities. Following this filtering, our dataset contained 737,521 dunes in 51,307 images.

Finally, we compute the average migration direction of all remaining detected dunes in each CTX image, weighting their individual migration vectors by the detection certainty (an output of the CNN) and the depth of the slipface convexity defect (as barchans with well-developed horns are more easily interpreted), and bin the results in  $10^\circ \times 10^\circ$  bins between  $-70^\circ\text{N}$  and  $70^\circ\text{N}$ , and  $2^\circ \times 2^\circ$  bins poleward of  $70^\circ\text{N}$  (where dunes are more abundant). To validate this method, we compared the migration direction of terrestrial barchan dunes, derived from satellite images and our automatic method to in-situ measurements of sand flux direction (Figure S1; Supplementary Materials).

## 2.2 Net-Sand Flux Direction from GCMs

To compare our results with GCM predictions, we computed the net sand-flux direction using outputs from (1) Laboratoire de Météorologie Dynamique (LMD) simulations archived in the Mars Climate Database (MCD; Forget et al., 1999; Millour et al., 2018), and (2) Mars Weather and Research Forecasting (MarsWRF; Richardson et al., 2007) simulations (Supplementary Materials). From these, we extracted wind shear velocity ( $u_*$ ), atmospheric density at the surface

( $\rho_f$ ), and average wind azimuth ( $\theta$ ) at a height of 1 m above the surface. For LMD simulations, outputs were binned spatially at  $5^\circ$  and temporally in intervals of  $30^\circ$  solar longitude, whereas MarsWRF outputs were binned spatially at  $5^\circ$  and temporally in intervals of 1 hour. Next, we calculate the net sand-flux direction,  $\bar{\theta}_m$ , as the average wind azimuth weighted by the magnitude of the saltation flux vector,  $q_s$ , i.e.,

$$\bar{\theta}_m = \arctan\left(\frac{\bar{S}}{\bar{C}}\right)$$

where,

$$\bar{S} = \frac{\int \sin(\theta(t)) q_s(t) dt}{\int q_s(t) dt}; \quad \bar{C} = \frac{\int \cos(\theta(t)) q_s(t) dt}{\int q_s(t) dt} \quad (\text{Eq. 1})$$

Decades of experimental and field studies of aeolian sand transport have led to the formulation of numerous empirical saltation-flux laws (Kok et al., 2012). We conducted the calculations in Equation 1 using the semi-empirical saltation-flux law Martin & Kok (2017),

$$q_s \propto \rho_f u_{*it} (u_*^2 - u_{*it}^2) \quad (\text{Eq. 2})$$

where  $u_{*it} \approx 0.7 \text{ m s}^{-1}$  is the effective impact threshold for sand transport as relevant to modeling at 10–100 km spatial scales on Mars (Ayoub et al., 2014). Whereas we chose to illustrate our results with this commonly used flux law, we found results to be insensitive to the choice of the flux law (e.g., Werner, 1990) and the chosen impact threshold, which was varied in the range  $0 - 1 \text{ m s}^{-1}$ . As a result, the different temporal resolutions of the two GCMs, which may in principle affect calculated fluxes, does not significantly affect calculated net sand-flux directions. Finally, estimates of  $\bar{\theta}_m$  from GCM outputs were binned to match the resolution of measured barchan-migration directions.

### 3 Results: Global Dune Migration Directions

We find that dune-migration direction is dominantly to the east at latitudes  $> 45^\circ\text{N}$ , whereas it is mostly to the south between  $-45^\circ\text{N}$  and  $45^\circ\text{N}$ . Furthermore, dune migration directions follow continuous streamlines over thousands of kilometers over much of the surface of Mars (Figure 2a), some of which appear to mimic the routes of dust storms as previously mapped for Mars Years 24–32 (white dashed lines in Figure 5a; Battalio & Wang, 2021). The alignment between storm tracks and dune-migration direction suggests that, in many places, the same wind circulations are responsible for the propagation of dust storms and the migration of sand dunes. This hypothesis is further corroborated by the overlap between the seasonal windows of dust storms (solar longitudes  $L_s \sim 140\text{--}250^\circ$  globally, with secondary windows at  $300^\circ\text{--}360^\circ$  and  $10\text{--}70^\circ$  in the northern and southern hemispheres, respectively; Battalio & Wang, 2021) and the seasonality of sand transport as observed on the ground and from orbit (e.g.,  $L_s \sim 200^\circ\text{--}10^\circ$  in Gale

crater and  $\sim 200^{\circ}$ – $350^{\circ}$  in Nili Patera; (Ayoub et al., 2014; Baker, Lapôtre, et al., 2018; Baker, Newman, et al., 2018; Bridges et al., 2017; Lapôtre & Rampe, 2018). Whereas our data and analysis does not confirm any causal relationship, the correlation between dust-storm tracks and sand-transport pathways hints at the role of saltation in lofting finer dust and initiating dust storms on Mars (Greeley, 2002; Newman et al., 2002; Pollack et al., 1976).

At high northern latitudes (Figure 5b), dune migration directions largely follow Mars' polar vortex circulation (Lancaster & Greeley, 1990), with an additional southward component that appears to be pervasive across the north polar region. We find good agreement between our results and previously manually mapped barchan migration directions (Ward et al., 1985). Additionally, we identify two major surface wind convergence zones near the north pole using the dune orientations: (1) at the southern end of Chasma Boreale (labeled “f” in Figure 2b), and (2) between polar cyclonic and anti-cyclonic flows ( $\sim 85^{\circ}\text{N}$ ,  $-120$ – $120^{\circ}\text{E}$ ; Olympia Undae). These wind convergence zones are likely responsible for observed enhanced dune sizes in those regions (Rubanenko et al., 2022).

Most of the ground-based wind and sand-flux measurements on Mars (yellow arrows in Figure 5a) agree with our machine-learning-derived migration directions. Where winds were measured directly on the ground, any disagreements is explained by the influence of local topographic winds (e.g., at the Viking 1, Curiosity, and Insight landing sites; Baker et al., 2022; Banfield et al., 2020; Hess et al., 1977).

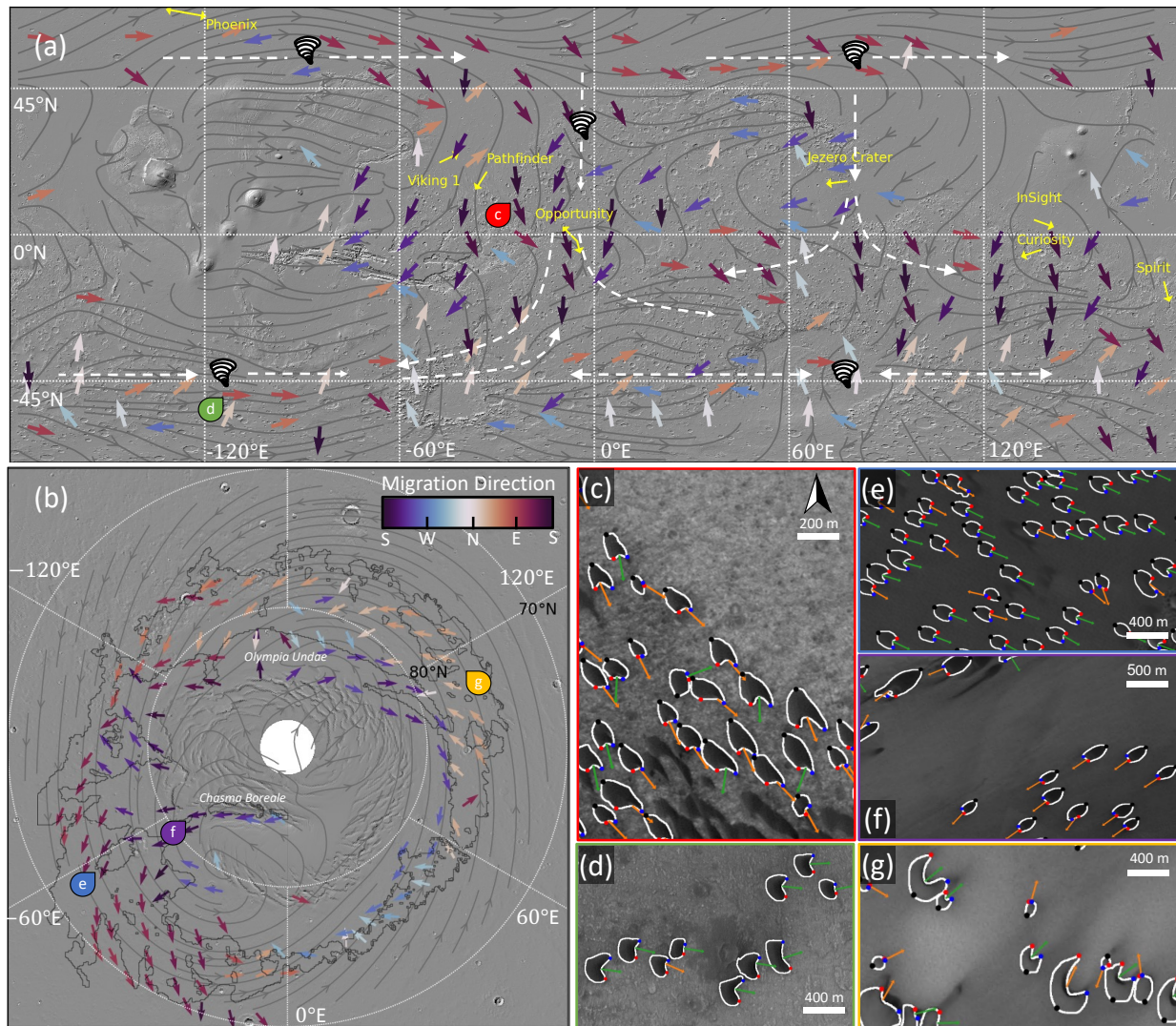


Figure 4: Map of barchan dune migration directions on Mars derived using machine learning overlain on MOLA shaded relief (a) at  $-70^{\circ}N$ - $70^{\circ}N$  latitudes, binned at  $10^{\circ} \times 10^{\circ}$ ; white dashed vectors and vortices represent dust-storm paths (after Battalio & Wang, 2021); and (b) at latitudes  $> 70^{\circ}N$ , binned at  $2^{\circ} \times 2^{\circ}$ . Yellow arrows with labels indicate local estimates of wind or sand flux direction from landed spacecraft (Supplementary Materials). Gray streamlines are LMD-derived migration directions (Forget et al., 1999). (c-g) Machine-learning-derived dune outlines and derived migration vectors for individual dunes overlain on CTX imagery. Green and orange arrows are the estimated migration vectors from bisector (symmetric dunes) and tail-slipface vector (asymmetric dunes), respectively. Note that for dunes with short horns, these two methods produce relatively similar results. North is up in (c-g). Image coordinates: (c)  $15.1^{\circ}N, -22.18^{\circ}E$  (d)  $-47.31^{\circ}N, -115.06^{\circ}E$  (e)  $73.86^{\circ}N, -45.12^{\circ}E$  (f)  $84.7^{\circ}N, -31.3^{\circ}E$  (g)  $76.52^{\circ}N, 105.05^{\circ}E$ . Phoenix' bidirectional arrow indicates the seasonal variation in wind direction measured by the lander's anemometer. Black contour in panel (b) shows the extent of manually mapped dune fields (Hayward et al., 2007).

## 4 Discussion

### 4.1 Global Sand Flux Predictions by GCMs

The net-sand flux directions computed by the two GCMs (streamlines in Figures 2 and S2) generally agree with observed dune-migration directions, and mostly disagree in areas with large topographic relief or gradients, such as near Valles Marineris (-13.9°N, -59.2°E), the Hellas (-42.4°N, 70.5°E) and Argyre (-49.5°N, 136.0°E) impact basins, or near the dichotomy boundary (Section 4.2). In other places, such as in northern Terra Sabaea from Meridiani Planum to Syrtis Major (approximately 0 – 45°N; 0 – 60°E), GCM predictions are poorly aligned with (and in places are even opposite to) measured dune-migration directions – even though the dunes themselves appear to follow continuous streamlines. Inspection of repeat High Resolution Imaging Experiment (HiRISE) imagery (Chojnacki et al., 2019) reveals that the modern migration direction of meter-scale ripples, superimposed onto the barchan dunes, agrees with inferred dune-migration direction, thus ruling out the possibility that dune morphology in that region does not reflect contemporaneous wind conditions. This discrepancy points to potential limitations of GCM predictions. Another notable example of potential disagreement between GCM predictions and observations is the presence of an anti-cyclonic “inner ring” of barchans migrating west poleward of 78°N (purple-blue arrows in Figure 5b), which was also identified by Tsoar et al. (1979) and Ward et al. (1985) but does not appear to be resolved by GCMs. We speculate that this wind corridor, proximal to the ice cap, may be linked to topographic winds emerging from the polar ice cap (Ewing & Kocurek, 2010; Spiga & Smith, 2018; Tsoar et al., 1979). This hypothesis is supported by the slight but pervasive southward component of dune migration vectors within that

corridor (Figure 5b). We do not identify any systematic differences in the performance of the two GCMs; they appear to provide equally overall accurate predictions of net sand-transport pathways

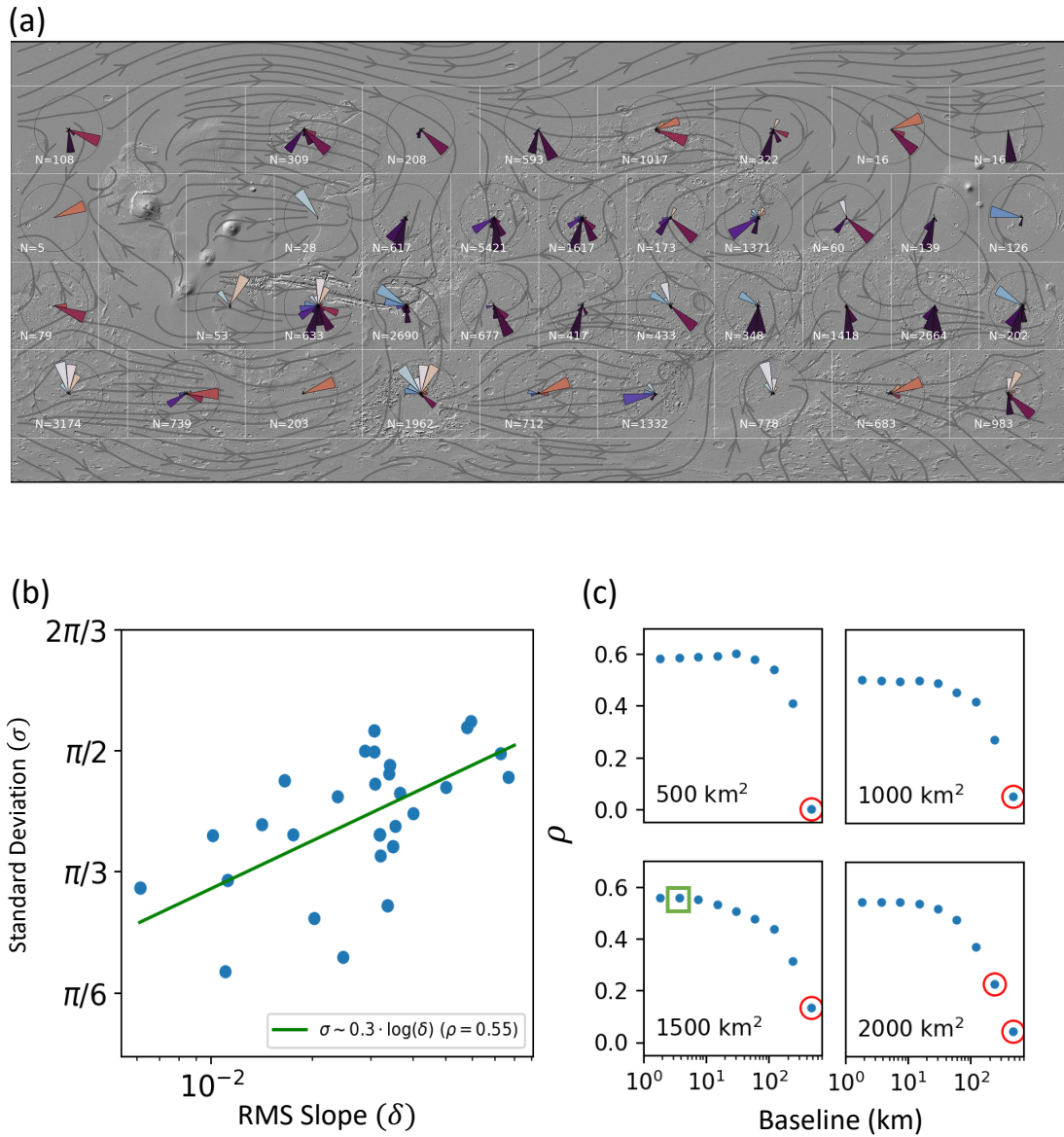


Figure 6: (a) Rose diagrams of dune-migration directions, binned in  $1,500 \text{ km}^2$  equal-area bins. (b) Correlation between the RMS slope of topography,  $\delta$ , and the standard deviation of dune-migration directions,  $\sigma$ , within each spatial bin (bin area =  $1,500 \text{ km}^2$ , baseline =  $4 \text{ km}$ ). N values indicate the number of dunes within each bin. (c) Correlation coefficient,  $\rho$ , between  $\sigma$  and  $\delta$  as calculated for different bin sizes (labeled within each panel) and topographic baselines (x-axis). Red circles indicate non-significant ( $p > 0.05$ ; Wald test) correlations. Green square highlights the example correlation shown in (b).

## 4.2 Influence of Topography on Surface Winds

Topographic roughness from micro- to planetary scales may affect the magnitude and direction of surface winds. Specifically, deviations in wind direction from its regional trend, e.g., caused by impact craters, may result in a local misalignment between barchan migration direction and regional winds. Such deviations are notably observed in regions characterized by high topographic relief, such as Valles Marineris and the Isidis and Hellas basins, as evidenced by a larger dispersion in dune migration direction within adjacent dune fields in those regions (**Error! Reference source not found.a**).

To quantify the relationship between wind dispersion and topography, dune-migration data were binned spatially in equal-area bins. We correlated the Yamartino (angular) standard deviation of observed dune-migration directions ( $\sigma$ ) with the root mean square (RMS) slope ( $\delta$ ) derived from Mars Orbiter Laser Altimeter (MOLA; Fergason et al., 2018; Smith et al., 2001) data within each bin, resampled over a given distance, which determines the topographic baseline (the horizontal scale of the considered topographic roughness). A stronger correlation (higher correlation coefficient) between  $\sigma$  and  $\delta$  could imply that increased topographic roughness leads to a greater dispersion in dune migration directions; i.e., that the presence of topographic roughness impacts the direction of surface winds that drive dune migration. Increasing the spatial bin size increases the number of dunes within that bin, thus decreasing the statistical error in calculating  $\sigma$  and  $\delta$ , but it also leads to fewer ( $\delta, \sigma$ ) pairs from which the correlation is calculated, negatively impacting the significance of any correlations. To explore this tradeoff, we performed the analysis for wide ranges of spatial bin sizes (500–2,000 km<sup>2</sup>) and topographic baselines (2–500 km) (**Error! Reference source not found.b**).

Regardless of spatial bin size, we find a consistent correlation between  $\sigma$  and  $\delta$  for topographic baselines smaller than ~10-50 km (**Error! Reference source not found.b, c**), suggesting that at those scales, dune migration is influenced by winds induced or diverted by local topography (Chojnacki et al., 2019; Ewing & Kocurek, 2010; Hess et al., 1977; Parteli et al., 2014). The strength of the correlation between  $\sigma$  and  $\delta$  decreases with the topographic baseline, until it ceases to be statistically significant for horizontal scales > 100 km. This implies that at scales < 100 km, topography affects the regional circulation. In turn, dune migration is more affected by Mars' global circulation, which would orient dunes in the same direction and decrease  $\sigma$ . For example, dune migration within topographic depressions (such as craters) > 100 km is more likely driven by regional circulation and not, e.g., by local slope winds or winds deflected by topographic obstacles (Ewing & Kocurek, 2010; Fenton et al., 2005; Gunn et al., 2022).

Martian impact craters trap sand, which often accumulates to form dune fields or windblow deposits (Gunn et al., 2022), some of them ancient and lithified (Banham et al., 2018, 2021; Day & Catling, 2020; Day & Dorn, 2019; Grotzinger et al., 2005; Lapôtre et al., 2016, 2021; Milliken et al., 2014; Rubin et al., 2022). We find that crater depth exerts a strong control over the potential distance between the center of dune fields and the center of the crater that hosts them, such that dunes within deep craters are typically found closer to the crater center. In contrast, dunes within shallower craters (but not necessarily smaller craters) typically accumulate near the crater wall (Figure 4a). Additionally, deep craters cause dune-migration direction to deviate from the average regional migration direction (Figure 4b), as estimated by binning migration direction in the same bins as in Figure 3. For example, an increase of an order of magnitude in crater depth increases the average difference between dune-migration direction within the crater and the average regional migration direction two-folds.

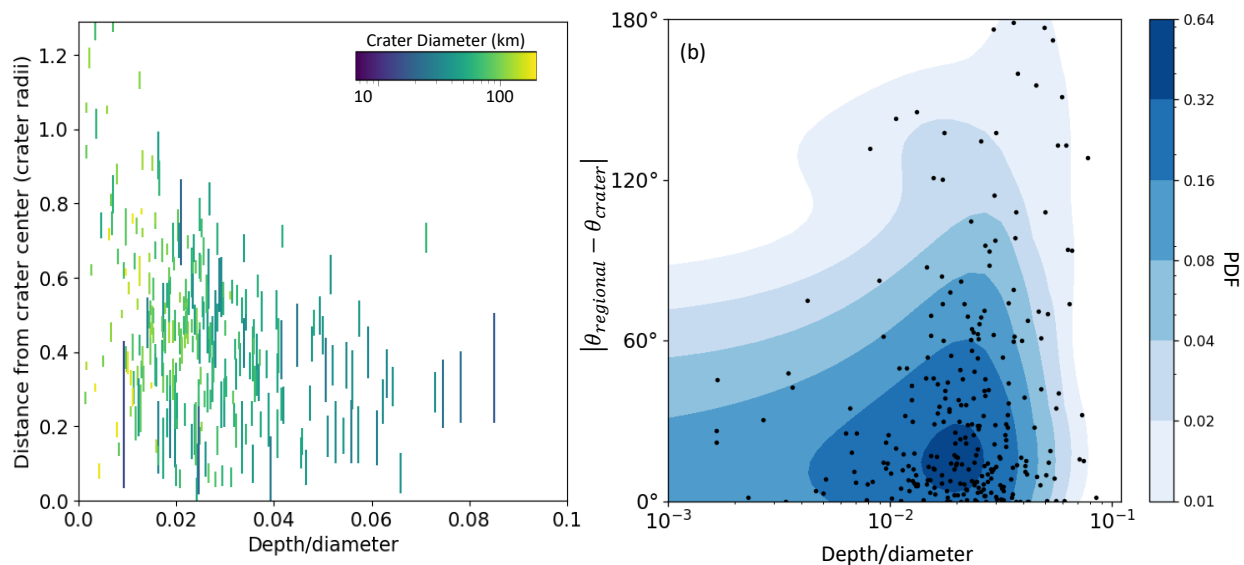


Figure 7: (a) Maximum distance between the center of mass of the dune field and the center of the crater decreases with crater depth. Error bars show the width of the dune field normalized by crater diameter. (b) Angular difference between the migration directions of intracrater dunes and dunes within the greater region outside of the crater. Migration direction of dunes within deep craters are more statistically likely to deviate from the direction of the regional migration directions (binned as in Figure 5).

## 5 Conclusion

The morphology of barchan dunes can be used to infer their migration directions as a proxy for the direction of the winds that shape them. We employed a neural network to map and outline barchan dunes globally on Mars. From dune outlines, we derived their orientation and their corresponding migration directions. In the absence of long-lived and global meteorological monitoring on Mars, our dataset provides a unique opportunity to investigate the planet’s modern (Figure S4) near-surface wind circulation on a global scale.

We find that dune migration on Mars follows continuous streamlines that extend for thousands of kilometers, indicating that dune migration on the planet is mainly dictated by its global atmospheric circulation. We find that dune migration is aligned with dust-storm tracks – possibly hinting at dust lifting by saltating sand – and in good agreement with ground-based wind direction or sand-flux constraints. Misalignments between dune-migration directions and direct

measurements can in all cases be explained by winds induced by local topography. Outputs from two GCMs (LMD and MarsWRF) compare similarly well to inferred net sand-flux directions, with a few exceptions, especially in regions of high topographic relief. Notably, the GCMs do not appear to resolve an anti-cyclonic wind corridor at the base of the north polar cap.

To quantify the influence of topography on dune-migration directions, we measured the topographic roughness at different horizontal baselines. We find that the dispersion in migration directions, quantified by the angular standard deviation, increases with the topographic roughness, quantified by the RMS slope. Specifically, we find that the topographic signature of impact craters significantly influences dune formation and migration. Dune fields found within deeper craters ( $d/D > 0.01$ ) tend to be located closer to the crater center, and display larger deviations from the average regional dune-migration direction.

We hypothesize that the strong influence of topographic roughness, craters, and ice-cap valleys on surface wind directions on Mars is rooted in the planet's large swings in near-surface atmospheric stability. In stably stratified boundary layers, surface winds are isolated from the geostrophic winds aloft and as a result, tend to be slower and guided by topographic features (Gadal et al., 2022). In contrast, surface winds in a convective boundary layer tend to be faster and have an outsized influence on sand transport (Gunn et al., 2021). Katabatic winds down the ice-cap valleys and some crater walls are expected to be strong on Mars due to such large diurnal variations in boundary-layer stability. Critically, these processes are challenging for GCMs to resolve due to parameterizations of non-equilibrium stability effects in the boundary layer, as well as spatial resolution. Our results are thus compelling evidence that discrepancies between observation and simulation manifest through the interaction of topography and the stability of the near-surface atmosphere on Mars. Therefore, caution needs to be applied when interpreting paleo-wind directions on Mars from ancient aeolian sandstones. As sedimentary sinks, many impact craters on Mars have preserved an aeolian sedimentary record. The strong influence of crater topography on sediment accumulation and wind direction is likely to be reflected in the stratigraphy of craters with diameters  $< 100$  km, and those strata may neither provide a direct record of regional winds nor be reproducible by current GCMs.

### Acknowledgments

This work was supported in part by NASA grants 80NSSC20K0145 to MGAL and 80NSSC21K1090 to RCE.

### Data Availability

Data used in this study can be accessed through this link:

[https://figshare.com/articles/dataset/dunes\\_migration\\_csv/21755843](https://figshare.com/articles/dataset/dunes_migration_csv/21755843)

### Code Availability

Code used to process the data is available here: <https://doi.org/10.5281/zenodo.7305150>.

## References

- Ayoub, F., Avouac, J.-P., Newman, C. E., Richardson, M. I., Lucas, A., Leprince, S., & Bridges, N. T. (2014). Threshold for sand mobility on Mars calibrated from seasonal variations of sand flux. *Nature Communications*, 5(1), 1–8.

- Baker, M. M., Newman, C. E., Lapotre, M. G. A., Sullivan, R., Bridges, N. T., & Lewis, K. W. (2018). Coarse sediment transport in the modern Martian environment. *JGR: Planets*, *123*(6), 1380–1394.
- Baker, M. M., Lapôtre, M. G. A., Minitti, M. E., Newman, C. E., Sullivan, R., Weitz, C. M., et al. (2018). The Bagnold Dunes in southern summer: Active sediment transport on Mars observed by the Curiosity rover. *Geophysical Research Letters*, *45*(17), 8853–8863.
- Baker, M. M., Newman, C. E., Sullivan, R., Minitti, M. E., Edgett, K. S., Fey, D., et al. (2022). Diurnal variability in aeolian sediment transport at Gale crater, Mars. *JGR: Planets*, *127*(2), e2020JE006734.
- Banfield, D., Spiga, A., Newman, C., Forget, F., Lemmon, M., Lorenz, R., et al. (2020). The atmosphere of Mars as observed by InSight. *Nature Geoscience*, *13*(3), 190–198.
- Banham, S. G., Gupta, S., Rubin, D. M., Watkins, J. A., Sumner, D. Y., Edgett, K. S., et al. (2018). Ancient Martian aeolian processes and palaeomorphology reconstructed from the Stimson formation on the lower slope of Aeolis Mons, Gale crater, Mars. *Sedimentology*, *65*(4), 993–1042.
- Banham, S. G., Gupta, S., Rubin, D. M., Edgett, K. S., Barnes, R., Van Beek, J., et al. (2021). A rock record of complex aeolian bedforms in a Hesperian desert landscape: the Stimson formation as exposed in the Murray buttes, Gale crater, Mars. *JGR: Planets*, *126*(4), e2020JE006554.
- Battalio, M., & Wang, H. (2021). The Mars Dust Activity Database (MDAD): A comprehensive statistical study of dust storm sequences. *Icarus*, *354*, 114059.
- Bourke, M. C., & Goudie, A. S. (2009). Varieties of barchan form in the Namib Desert and on Mars. *Aeolian Research*, *1*(1–2), 45–54. <https://doi.org/10.1016/j.aeolia.2009.05.002>
- Breed, C. S., Grolier, M. J., & McCauley, J. F. (1979). Morphology and distribution of common ‘sand’ dunes on Mars: Comparison with the Earth. *Journal of Geophysical Research: Solid Earth*, *84*(B14), 8183–8204.
- Bridges, N. T., Bourke, M. C., Geissler, P. E., Banks, M. E., Colon, C., Diniega, S., et al. (2012). Planet-wide sand motion on Mars. *Geology*, *40*(1), 31–34.
- Bridges, N. T., Sullivan, R., Newman, C. E., Navarro, S., Van Beek, J., Ewing, R. C., et al. (2017). Martian aeolian activity at the Bagnold Dunes, Gale Crater: The view from the surface and orbit. *JGR: Planets*, *122*(10), 2077–2110.
- Cantor, B. A., James, P. B., Caplinger, M., & Wolff, M. J. (2001). Martian dust storms: 1999 Mars orbiter camera observations. *Journal of Geophysical Research: Planets*, *106*(E10), 23653–23687.
- Chojnacki, M., Banks, M. E., Fenton, L. K., & Urso, A. C. (2019). Boundary condition controls on the high-sand-flux regions of Mars. *Geology*, *47*(5), 427–430.
- Day, M., & Catling, D. C. (2020). Potential aeolian deposition of intra-crater layering: A case study of Henry crater, Mars. *Bulletin*, *132*(3–4), 608–616.
- Day, M., & Dorn, T. (2019). Wind in Jezero crater, Mars. *Geophysical Research Letters*, *46*(6), 3099–3107.

- Dickson, J. L., Kerber, L. A., Fassett, C. I., & Ehlmann, B. L. (2018). A global, blended CTX mosaic of Mars with vectorized seam mapping: A new mosaicking pipeline using principles of non-destructive image editing. In *LPSC* (Vol. 49, pp. 1–2).
- Diniega, S., Bramson, A. M., Buratti, B., Buhler, P., Burr, D. M., Chojnacki, M., et al. (2021). Modern Mars' geomorphological activity, driven by wind, frost, and gravity. *Geomorphology*, *380*, 107627.
- Ewing, R. C., & Kocurek, G. A. (2010). Aeolian dune interactions and dune-field pattern formation: White Sands Dune Field, New Mexico. *Sedimentology*, *57*(5), 1199–1219.
- Ewing, R. C., Lapôtre, M. G. A., Lewis, K. W., Day, M., Stein, N., Rubin, D. M., et al. (2017). Sedimentary processes of the Bagnold Dunes: Implications for the eolian rock record of Mars. *Journal of Geophysical Research: Planets*, *122*(12), 2544–2573.
- Fenton, L. K. (2020). Updating the global inventory of dune fields on Mars and identification of many small dune fields. *Icarus*, *352*, 114018.
- Fenton, L. K., & Hayward, R. K. (2010). Southern high latitude dune fields on Mars: Morphology, aeolian inactivity, and climate change. *Geomorphology*, *121*(1–2), 98–121.
- Fenton, L. K., Toigo, A. D., & Richardson, M. I. (2005). Aeolian processes in Proctor Crater on Mars: Mesoscale modeling of dune-forming winds. *Journal of Geophysical Research: Planets*, *110*(E6).
- Ferguson, R. L., Hare, T. M., & Laura, J. (2018). HRSC and MOLA blended digital elevation model at 200m v2, astrogeology PDS annex. *US Geological Survey*.
- Forget, F., Hourdin, F., Fournier, R., Hourdin, C., Talagrand, O., Collins, M., et al. (1999). Improved general circulation models of the Martian atmosphere from the surface to above 80 km. *Journal of Geophysical Research: Planets*, *104*(E10), 24155–24175.
- Gadal, C., Delorme, P., Narteau, C., Wiggs, G. F. S., Baddock, M., Nield, J. M., & Claudin, P. (2022). Local wind regime induced by giant linear dunes: comparison of ERA5-land reanalysis with surface measurements. *Boundary-Layer Meteorology*, *185*(3), 309–332.
- Gao, X., Narteau, C., Rozier, O., & Du Pont, S. C. (2015). Phase diagrams of dune shape and orientation depending on sand availability. *Scientific Reports*, *5*(1), 1–12.
- Greeley, R. (2002). Saltation impact as a means for raising dust on Mars. *Planetary and Space Science*, *50*(2), 151–155.
- Greeley, R., White, B. R., Pollack, J. B., Iversen, J. D., & Leach, R. N. (1981). Dust storms on Mars: Considerations and simulations. *Spec. Pap. Geol. Soc. Am.*, *186*, 101–121.
- Grotzinger, J. P., Arvidson, R. E., Bell III, J. F., Calvin, W., Clark, B. C., Fike, D. A., et al. (2005). Stratigraphy and sedimentology of a dry to wet eolian depositional system, Burns formation, Meridiani Planum, Mars. *Earth and Planetary Science Letters*, *240*(1), 11–72.
- Gunn, A., Wanker, M., Lancaster, N., Edmonds, D. A., Ewing, R. C., & Jerolmack, D. J. (2021). Circadian rhythm of dune-field activity. *Geophysical Research Letters*, *48*(5), e2020GL090924.
- Gunn, A., Rubanenko, L., & Lapôtre, M. G. A. (2022). Accumulation of windblown sand in impact craters on Mars. *Geology*.

- Hayward, R. K., Mullins, K. F., Fenton, L. K., Hare, T. M., Titus, T. N., Bourke, M. C., et al. (2007). Mars global digital dune database and initial science results. *Journal of Geophysical Research: Planets*, 112(E11).
- Hayward, R. K., Fenton, L. K., Titus, T. N., Colaprete, A., & Christensen, P. R. (2012). Mars global digital dune database: MC-30. *US Geological Survey Open-File Report*, 1259.
- He, K., Gkioxari, G., Dollár, P., & Girshick, R. (2017). Mask R-CNN. *IEEE ICCV*.
- Hess, S. L., Henry, R. M., Leovy, C. B., Ryan, J. A., & Tillman, J. E. (1977). Meteorological results from the surface of Mars: Viking 1 and 2. *JGR*, 82(28), 4559–4574.
- Kite, E. S. (2019). Geologic constraints on early Mars climate. *Space Science Reviews*, 215(1), 1–47.
- Lancaster, N., & Greeley, R. (1990). Sediment volume in the north polar sand seas of Mars. *Journal of Geophysical Research: Solid Earth*, 95(B7), 10921–10927.
- Lapôtre, M. G. A., & Rampe, E. B. (2018). Curiosity’s investigation of the Bagnold Dunes, Gale crater: Overview of the two-phase scientific campaign and introduction to the special collection. *Geophysical Research Letters*, 45(19), 10–200.
- Lapôtre, M. G. A., Ewing, R. C., Lamb, M. P., Fischer, W. W., Grotzinger, J. P., Rubin, D. M., et al. (2016). Large wind ripples on Mars: A record of atmospheric evolution. *Science*, 353(6294), 55–58.
- Lapôtre, M. G. A., O’Rourke, J. G., Schaefer, L. K., Siebach, K. L., Spalding, C., Tikoo, S. M., & Wordsworth, R. D. (2020). Probing space to understand Earth. *Nature Reviews Earth & Environment*, 1(3), 170–181.
- Lapôtre, M. G. A., Ewing, R. C., & Lamb, M. P. (2021). An evolving understanding of enigmatic large ripples on Mars. *Journal of Geophysical Research: Planets*, 126(2), e2020JE006729.
- Levine, J. S., Kerschmann, R. L., & Winterhalter, D. (2018). *Dust in the atmosphere of Mars and its impact on human exploration*. Cambridge Scholars Publishing.
- Malin, M. C., Bell, J. F., Cantor, B. A., Caplinger, M. A., Calvin, W. M., Clancy, R. T., et al. (2007). Context camera investigation on board the Mars Reconnaissance Orbiter. *Journal of Geophysical Research: Planets*, 112(E5).
- Martin, R. L., & Kok, J. F. (2017). Wind-invariant saltation heights imply linear scaling of aeolian saltation flux with shear stress. *Science Advances*, 3(6), e1602569.
- Milliken, R. E., Ewing, R. C., Fischer, W. W., & Hurowitz, J. (2014). Wind-blown sandstones cemented by sulfate and clay minerals in Gale Crater, Mars. *Geophysical Research Letters*, 41(4), 1149–1154.
- Millour, E., Forget, F., Spiga, A., Vals, M., Zakharov, V., & Montabone, L. (2018). Mars climate database. In *From Mars Express to ExoMars, 27-28 February 2018, Madrid, Spain*.
- Montabone, L., & Forget, F. (2018). On forecasting dust storms on Mars. 48th International Conference on Environmental Systems.
- Newman, C. E., Lewis, S. R., Read, P. L., & Forget, F. (2002). Modeling the Martian dust cycle, 1. Representations of dust transport processes. *JGR: Planets*, 107(E12), 1–6.

- Parteli, E. J. R., Durán, O., Bourke, M. C., Tsoar, H., Pöschel, T., & Herrmann, H. (2014). Origins of barchan dune asymmetry: Insights from numerical simulations. *Aeolian Research*, *12*, 121–133.
- Pollack, J. B., Haberle, R., Greeley, R., & Iversen, J. (1976). Estimates of the wind speeds required for particle motion on Mars. *Icarus*, *29*(3), 395–417.
- Richardson, M. I., Toigo, A. D., & Newman, C. E. (2007). PlanetWRF: A general purpose, local to global numerical model for planetary atmospheric and climate dynamics. *JGR: Planets*, *112*(E9).
- Rubanenko, L., Pérez-López, S., Schull, J., & Lapôtre, M. G. A. (2021). Automatic Detection and Segmentation of Barchan Dunes on Mars and Earth Using a Convolutional Neural Network. *IEEE Journal of Selected Topics in Applied Earth Observations and Remote Sensing*, *14*, 9364–9371.
- Rubanenko, L., Lapotre, M. G. A., Ewing, R. C., Fenton, L. K., & Gunn, A. (2022). A distinct ripple-formation regime on Mars revealed by the morphometrics of barchan dunes. *Nature Communications*.
- Rubin, D. M., Lapôtre, M. G. A., Stevens, A. W., Lamb, M. P., Fedo, C. M., Grotzinger, J. P., et al. (2022). Ancient Winds, Waves, and Atmosphere in Gale Crater, Mars, Inferred From Sedimentary Structures and Wave Modeling. *Journal of Geophysical Research: Planets*, e2021JE007162.
- Smith, D. E., Zuber, M. T., Frey, H. V., Garvin, J. B., Head, J. W., Muhleman, D. O., et al. (2001). Mars Orbiter Laser Altimeter: Experiment summary after the first year of global mapping of Mars. *Journal of Geophysical Research: Planets*, *106*(E10), 23689–23722.
- Spiga, A., & Smith, I. (2018). Katabatic jumps in the Martian northern polar regions. *Icarus*, *308*, 197–208.
- Tsoar, H., & Parteli, E. J. R. (2016). Bidirectional winds, barchan dune asymmetry and formation of seif dunes from barchans: a discussion. *Environmental Earth Sciences*, *75*(18), 1–10.
- Tsoar, H., Greeley, R., & Peterfreund, A. R. (1979). Mars: The north polar sand sea and related wind patterns. *Journal of Geophysical Research: Solid Earth*, *84*(B14), 8167–8180.
- Ward, A. W., Doyle, K. B., Helm, P. J., Weisman, M. K., & Witbeck, N. E. (1985). Global map of eolian features on Mars. *Journal of Geophysical Research: Solid Earth*, *90*(B2), 2038–2056.
- Werner, B. T. (1990). A steady-state model of wind-blown sand transport. *The Journal of Geology*, *98*(1), 1–17.
- Wordsworth, R. D. (2016). The climate of early Mars. *Annual Review of Earth and Planetary Sciences*, *44*, 381–408.
- Zuber, M. T. (2003). Learning to think like martians. *Science*, *302*(5651), 1694–1695.

## **Global Surface Winds and Aeolian Sediment Pathways on Mars from the Morphology of Barchan Dunes**

**L. Rubanenko<sup>1,2</sup>, A. Gunn<sup>1,3</sup>, S. Pérez-López<sup>1</sup>, L.K. Fenton<sup>4</sup>, R.C. Ewing<sup>5</sup>, A. Soto<sup>6</sup> and M.G.A Lapôtre<sup>1</sup>**

<sup>1</sup> Department of Earth & Planetary Sciences, Stanford University, Stanford, California, USA.

<sup>2</sup> Civil and Environmental Engineering, Technion, Haifa, Israel.

<sup>3</sup> School of Earth, Atmosphere & Environment, Monash University, Clayton, Australia.

<sup>4</sup> Carl Sagan Center, SETI Institute, Mountain View, California, USA.

<sup>5</sup> Department of Geology & Geophysics, Texas A&M, College Station, Texas, USA.

<sup>6</sup> Southwest research Institute, Boulder, Colorado, USA.

Corresponding author: Lior Rubanenko ([liorr@stanford.edu](mailto:liorr@stanford.edu))

### **Key Points:**

- We derive global barchan dune migration directions on Mars using a convolutional neural network
- Aeolian sediment pathways on Mars are largely controlled by the planet's global circulation
- Surface winds are locally deflected by topographic obstacles < 100 km horizontal scales.

## Abstract

In the absence of consistent meteorological data on Mars, the morphology of dunes can be employed to study its atmosphere. Specifically, barchan dunes, which form under approximately unimodal winds, are reliable proxies for the dominant wind direction. Here, we characterize near-surface winds on Mars from the morphology of  $>10^6$  barchans mapped globally on the planet by a convolutional neural network. Barchan migration is predominantly aligned with the global circulation – northerly at mid-latitudes and cyclonic near the north pole – with the addition of an anti-cyclonic north-polar component that likely originates from winds emerging from the ice cap. Locally, migration directions deviate from regional trends in areas with high topographic roughness. Notably, obstacles  $<100$  km such as impact craters are efficient at deflecting surface winds. Our database, which provides insights into planetary-scale aeolian processes on modern-day Mars, can be used to constrain global circulation models to assist with predictions for future missions.

## Plain Language Summary

Crescent-shaped sand dunes are prevalent across the deserts of Mars. Here, we use the physical relationship between the shape of these dunes and the winds that form them to infer the directions of surface winds on Mars on a global scale. We find that dunes typically adhere to the global circulation patterns of Mars' atmosphere, and that local topographic winds are mostly important in areas with high topographic roughness such as inside deep impact craters. Our global wind map can serve to calibrate numerical climate models, which in turn can help us learn about the recent and modern-day climate of Mars.

## 1 Introduction

Winds have been a dominant driver of geologic activity on Mars, setting the pace of landscape erosion (Chojnacki et al., 2019), sediment transport and deposition (Baker et al., 2018; Bridges et al., 2012; Gunn et al., 2022), and controlling dust lifting (Greeley et al., 1981; Newman et al., 2004). Understanding the global circulation of modern surface winds is therefore not only important to model present-day atmospheric phenomena such as global dust storms in preparation for future crewed mission (e.g., Cantor et al., 2001; Greeley et al., 1981; Levine et al., 2018; Montabone & Forget, 2018), but also to calibrate global climate models (GCMs) that could then be used to decipher the planet's climatic record (Banham et al., 2018, 2021; Day & Dorn, 2019; Ewing et al., 2017; Fenton et al., 2005; Fenton & Hayward, 2010; Hayward et al., 2007; Kite, 2019; Lapôtre et al., 2020, 2021; Rubin et al., 2022; Tsoar et al., 1979; Ward et al., 1985; Wordsworth, 2016).

Crescentic (or barchan) dunes, which form under roughly unimodal winds in regions of limited sand supply, are widespread across the modern arid landscapes of Mars (Breed et al., 1979; Diniega et al., 2021; Fenton, 2020; Hayward et al., 2007, 2012; Rubanenko et al., 2021). The morphology of actively migrating barchan dunes can be used to infer the dominant wind direction and aeolian sediment transport pathways. The crestline orientation near the slipface center and horn orientations of actively migrating barchan dunes indicate the dominant wind and sediment transport directions (Figure 1; e.g., Gao et al., 2015). In some cases, the horns can become asymmetric, e.g., in the presence of a secondary wind component, as a result of dune-dune interactions, or topography (Bourke & Goudie, 2009; Parteli et al., 2014; Tsoar & Parteli, 2016). Thus, orbiter observations of barchan dunes have been used to indirectly characterize surface winds on Mars, where meteorological data is scarce (Hayward et al., 2007, 2012; Tsoar et al.,

1979). However, the majority of investigations that mapped individual dune migration directions focused on local-regional phenomena, as examining individual dunes globally has remained challenging (Ward et al., 1985). In contrast, the global database of Hayward et al. (2012) reports average slipface azimuths from  $\sim 10,000$  measurements,  $\sim 25\%$  of which were barchans.

Here, we expand the database of mapped barchan dunes by using higher resolution Mars Reconnaissance Orbiter Context Camera images (MRO CTX, Malin et al., 2007) as well as including recently mapped smaller dune fields (Fenton, 2020), which allows us to include barchan dunes in non-polar latitudes. We analyze a global dataset of barchan-dune outlines previously mapped on Mars by a convolutional neural network (Rubanenko et al., 2021). From dune outlines, we infer the orientation of dune slip-faces and horns (and their asymmetry) to infer local and global barchan migration patterns, driven by Mars' dominant near-surface winds and aeolian sediment transport pathways on a planetary scale. We further quantify the influence of topography on local winds by analyzing horn asymmetry and deviations between local dune migration direction and modeled regional winds. Altogether, our results provide a new global view of wind-driven sand transport on modern Mars that could be used to benchmark and refine GCM simulations of Mars' winds.

## 2 Methods

### 2.1 Automatic Measurement of Dune-Migration Direction

A convolutional neural network (CNN) is a type of machine learning technique that excels at tasks that require abstraction, such as object detection and segmentation in images. The CNN we employ in this study, Mask R-CNN (He et al., 2017), outlines objects in images by generalizing from a manually labeled dataset through an optimization process called *training*. Here, we employ a dataset of barchan dunes' outlines compiled by Rubanenko et al. (2021), who trained Mask R-CNN on images of barchan dunes tiled from the global MRO CTX mosaic (5 m/px) of Dickson et al. (2018). The trained model, which achieved a detection mean average precision of 77%, was used to automatically outline barchan dunes across the surface of Mars.

To spare computation time, and since the goal was to characterize known dunes and not to detect new ones, Rubanenko et al. (2021) focused on regions that were found to contain dune fields in previous investigations (Fenton, 2020; Hayward et al., 2007) between latitudes  $-70^{\circ}\text{N}$  and  $70^{\circ}\text{N}$ . Poleward of  $\pm 70^{\circ}\text{N}$ , all CTX images were inspected for the presence of barchan dunes. Through this process, the CNN detected over a million individual isolated barchan dunes on Mars, which were subsequently filtered to increase the robustness of the results (Rubanenko et al., 2022; Supplementary Materials). After manually reviewing a representative sample of the model detections, Rubanenko et al. (2022) elected to ignore any detections poleward of  $-70^{\circ}\text{N}$  due to the presence of sublimation-related features, such as spiders (Zuber, 2003), which the model occasionally misclassified as barchan dunes.

To measure the migration direction of a single barchan dune, we follow the procedure developed in Rubanenko et al. (2022). The algorithm automatically identifies six reference points

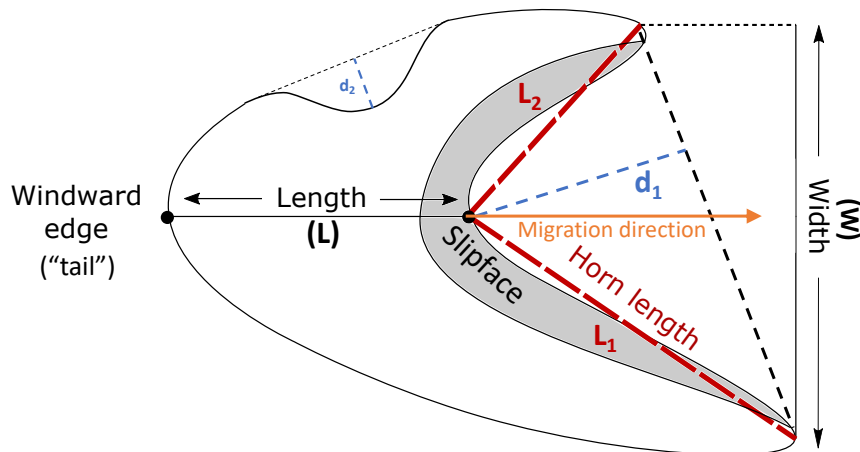


Figure 1: Definition of morphometric parameters. The dune slipface is identified as the deepest convexity defect along the dune contour (e.g.,  $d_1 > d_2$ ), and horns lengths ( $L_1$  and  $L_2$ ) are measured as the distance between the slipface and the horn apices.

along the dune contour: the center of the slipface, the two horn apices, the “tail” (upwind edge of the stoss) and sides. For relatively symmetric dunes (arbitrarily defined here as horn length ratio  $\max(L_1, L_2)/\min(L_1, L_2) < 2$ ), the migration direction is estimated as the bisector vector to the angle formed by the slipface center and horn apices (e.g., green arrows in Figure 2c–g). For asymmetric dunes ( $\max(L_1, L_2)/\min(L_1, L_2) > 2$ ), the migration direction was approximated to be in the direction of the line that links the tail to the slipface center (e.g., orange arrows in Figure 2c–g). To improve the robustness of our results, we further removed dunes with convexity defects  $< 2.5\%$  the dune length ( $L$  in Figure 1), and dunes for which the ratio between the second-deepest and deepest convexity defects ( $d_2/d_1$  Figure 1) exceeds 10%. The latter condition removed dunes with noisy contours, either due to mis-segmentation by the model or from natural complexities. Following this filtering, our dataset contained 737,521 dunes in 51,307 images.

Finally, we compute the average migration direction of all remaining detected dunes in each CTX image, weighting their individual migration vectors by the detection certainty (an output of the CNN) and the depth of the slipface convexity defect (as barchans with well-developed horns are more easily interpreted), and bin the results in  $10^\circ \times 10^\circ$  bins between  $-70^\circ\text{N}$  and  $70^\circ\text{N}$ , and  $2^\circ \times 2^\circ$  bins poleward of  $70^\circ\text{N}$  (where dunes are more abundant). To validate this method, we compared the migration direction of terrestrial barchan dunes, derived from satellite images and our automatic method to in-situ measurements of sand flux direction (Figure S1; Supplementary Materials).

## 2.2 Net-Sand Flux Direction from GCMs

To compare our results with GCM predictions, we computed the net sand-flux direction using outputs from (1) Laboratoire de Météorologie Dynamique (LMD) simulations archived in the Mars Climate Database (MCD; Forget et al., 1999; Millour et al., 2018), and (2) Mars Weather and Research Forecasting (MarsWRF; Richardson et al., 2007) simulations (Supplementary Materials). From these, we extracted wind shear velocity ( $u_*$ ), atmospheric density at the surface

( $\rho_f$ ), and average wind azimuth ( $\theta$ ) at a height of 1 m above the surface. For LMD simulations, outputs were binned spatially at  $5^\circ$  and temporally in intervals of  $30^\circ$  solar longitude, whereas MarsWRF outputs were binned spatially at  $5^\circ$  and temporally in intervals of 1 hour. Next, we calculate the net sand-flux direction,  $\bar{\theta}_m$ , as the average wind azimuth weighted by the magnitude of the saltation flux vector,  $q_s$ , i.e.,

$$\bar{\theta}_m = \arctan\left(\frac{\bar{S}}{\bar{C}}\right)$$

where,

$$\bar{S} = \frac{\int \sin(\theta(t)) q_s(t) dt}{\int q_s(t) dt}; \quad \bar{C} = \frac{\int \cos(\theta(t)) q_s(t) dt}{\int q_s(t) dt} \quad (\text{Eq. 1})$$

Decades of experimental and field studies of aeolian sand transport have led to the formulation of numerous empirical saltation-flux laws (Kok et al., 2012). We conducted the calculations in Equation 1 using the semi-empirical saltation-flux law Martin & Kok (2017),

$$q_s \propto \rho_f u_{*it} (u_*^2 - u_{*it}^2) \quad (\text{Eq. 2})$$

where  $u_{*it} \approx 0.7 \text{ m s}^{-1}$  is the effective impact threshold for sand transport as relevant to modeling at 10–100 km spatial scales on Mars (Ayoub et al., 2014). Whereas we chose to illustrate our results with this commonly used flux law, we found results to be insensitive to the choice of the flux law (e.g., Werner, 1990) and the chosen impact threshold, which was varied in the range  $0 - 1 \text{ m s}^{-1}$ . As a result, the different temporal resolutions of the two GCMs, which may in principle affect calculated fluxes, does not significantly affect calculated net sand-flux directions. Finally, estimates of  $\bar{\theta}_m$  from GCM outputs were binned to match the resolution of measured barchan-migration directions.

### 3 Results: Global Dune Migration Directions

We find that dune-migration direction is dominantly to the east at latitudes  $> 45^\circ\text{N}$ , whereas it is mostly to the south between  $-45^\circ\text{N}$  and  $45^\circ\text{N}$ . Furthermore, dune migration directions follow continuous streamlines over thousands of kilometers over much of the surface of Mars (Figure 2a), some of which appear to mimic the routes of dust storms as previously mapped for Mars Years 24–32 (white dashed lines in Figure 5a; Battalio & Wang, 2021). The alignment between storm tracks and dune-migration direction suggests that, in many places, the same wind circulations are responsible for the propagation of dust storms and the migration of sand dunes. This hypothesis is further corroborated by the overlap between the seasonal windows of dust storms (solar longitudes  $L_s \sim 140-250^\circ$  globally, with secondary windows at  $300^\circ-360^\circ$  and  $10-70^\circ$  in the northern and southern hemispheres, respectively; Battalio & Wang, 2021) and the seasonality of sand transport as observed on the ground and from orbit (e.g.,  $L_s \sim 200^\circ-10^\circ$  in Gale

crater and  $\sim 200^{\circ}$ – $350^{\circ}$  in Nili Patera; (Ayoub et al., 2014; Baker, Lapôtre, et al., 2018; Baker, Newman, et al., 2018; Bridges et al., 2017; Lapôtre & Rampe, 2018). Whereas our data and analysis does not confirm any causal relationship, the correlation between dust-storm tracks and sand-transport pathways hints at the role of saltation in lofting finer dust and initiating dust storms on Mars (Greeley, 2002; Newman et al., 2002; Pollack et al., 1976).

At high northern latitudes (Figure 5b), dune migration directions largely follow Mars' polar vortex circulation (Lancaster & Greeley, 1990), with an additional southward component that appears to be pervasive across the north polar region. We find good agreement between our results and previously manually mapped barchan migration directions (Ward et al., 1985). Additionally, we identify two major surface wind convergence zones near the north pole using the dune orientations: (1) at the southern end of Chasma Boreale (labeled “f” in Figure 2b), and (2) between polar cyclonic and anti-cyclonic flows ( $\sim 85^{\circ}\text{N}$ ,  $-120$ – $120^{\circ}\text{E}$ ; Olympia Undae). These wind convergence zones are likely responsible for observed enhanced dune sizes in those regions (Rubanenko et al., 2022).

Most of the ground-based wind and sand-flux measurements on Mars (yellow arrows in Figure 5a) agree with our machine-learning-derived migration directions. Where winds were measured directly on the ground, any disagreements is explained by the influence of local topographic winds (e.g., at the Viking 1, Curiosity, and Insight landing sites; Baker et al., 2022; Banfield et al., 2020; Hess et al., 1977).

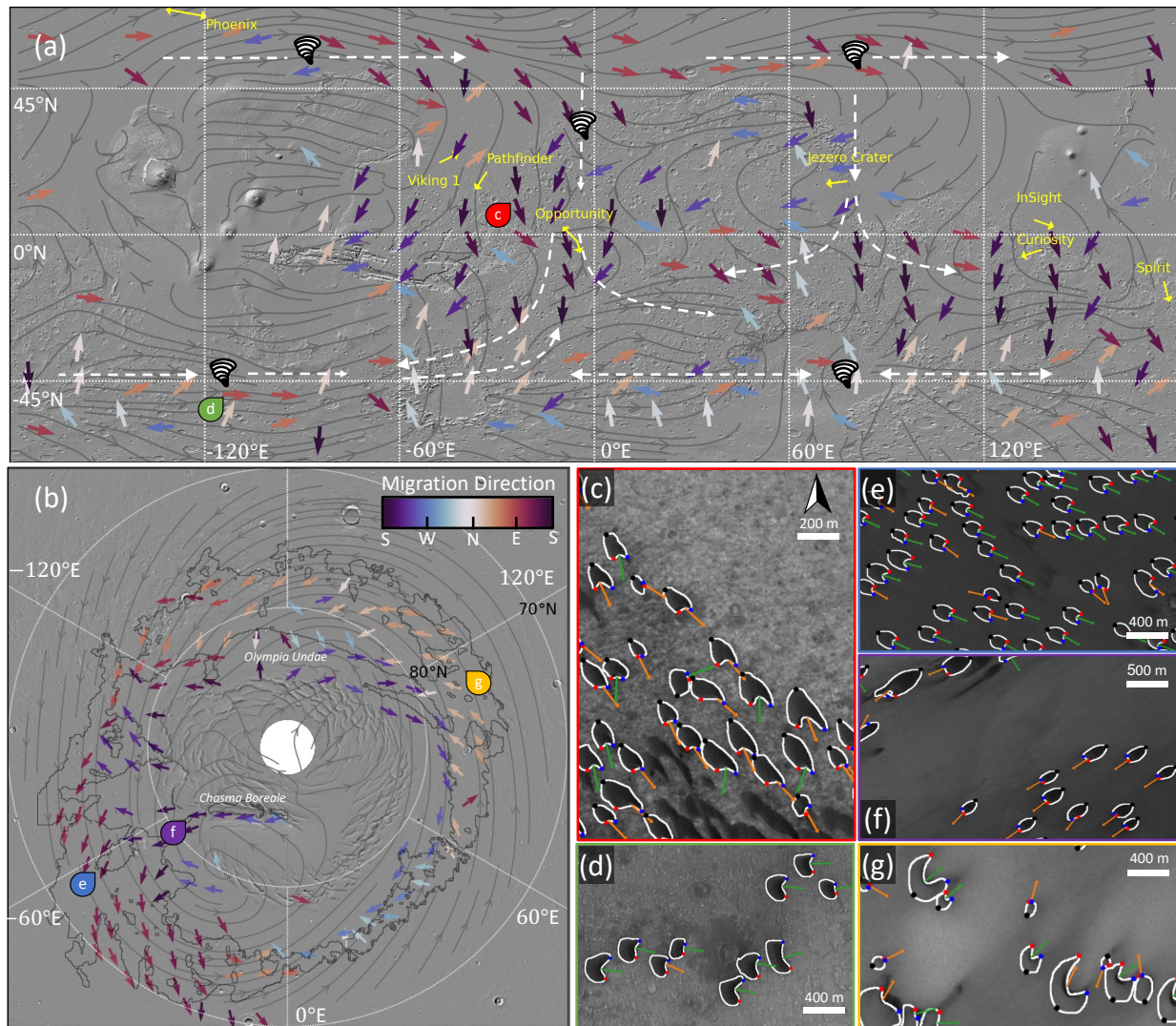


Figure 4: Map of barchan dune migration directions on Mars derived using machine learning overlain on MOLA shaded relief (a) at  $-70^{\circ}N$ - $70^{\circ}N$  latitudes, binned at  $10^{\circ} \times 10^{\circ}$ ; white dashed vectors and vortices represent dust-storm paths (after Battalio & Wang, 2021); and (b) at latitudes  $> 70^{\circ}N$ , binned at  $2^{\circ} \times 2^{\circ}$ . Yellow arrows with labels indicate local estimates of wind or sand flux direction from landed spacecraft (Supplementary Materials). Gray streamlines are LMD-derived migration directions (Forget et al., 1999). (c-g) Machine-learning-derived dune outlines and derived migration vectors for individual dunes overlain on CTX imagery. Green and orange arrows are the estimated migration vectors from bisector (symmetric dunes) and tail-slipface vector (asymmetric dunes), respectively. Note that for dunes with short horns, these two methods produce relatively similar results. North is up in (c-g). Image coordinates: (c)  $15.1^{\circ}N, -22.18^{\circ}E$  (d)  $-47.31^{\circ}N, -115.06^{\circ}E$  (e)  $73.86^{\circ}N, -45.12^{\circ}E$  (f)  $84.7^{\circ}N, -31.3^{\circ}E$  (g)  $76.52^{\circ}N, 105.05^{\circ}E$ . Phoenix' bidirectional arrow indicates the seasonal variation in wind direction measured by the lander's anemometer. Black contour in panel (b) shows the extent of manually mapped dune fields (Hayward et al., 2007).

## 4 Discussion

### 4.1 Global Sand Flux Predictions by GCMs

The net-sand flux directions computed by the two GCMs (streamlines in Figures 2 and S2) generally agree with observed dune-migration directions, and mostly disagree in areas with large topographic relief or gradients, such as near Valles Marineris (-13.9°N, -59.2°E), the Hellas (-42.4°N, 70.5°E) and Argyre (-49.5°N, 136.0°E) impact basins, or near the dichotomy boundary (Section 4.2). In other places, such as in northern Terra Sabaea from Meridiani Planum to Syrtis Major (approximately 0 – 45°N; 0 – 60°E), GCM predictions are poorly aligned with (and in places are even opposite to) measured dune-migration directions – even though the dunes themselves appear to follow continuous streamlines. Inspection of repeat High Resolution Imaging Experiment (HiRISE) imagery (Chojnacki et al., 2019) reveals that the modern migration direction of meter-scale ripples, superimposed onto the barchan dunes, agrees with inferred dune-migration direction, thus ruling out the possibility that dune morphology in that region does not reflect contemporaneous wind conditions. This discrepancy points to potential limitations of GCM predictions. Another notable example of potential disagreement between GCM predictions and observations is the presence of an anti-cyclonic “inner ring” of barchans migrating west poleward of 78°N (purple-blue arrows in Figure 5b), which was also identified by Tsoar et al. (1979) and Ward et al. (1985) but does not appear to be resolved by GCMs. We speculate that this wind corridor, proximal to the ice cap, may be linked to topographic winds emerging from the polar ice cap (Ewing & Kocurek, 2010; Spiga & Smith, 2018; Tsoar et al., 1979). This hypothesis is supported by the slight but pervasive southward component of dune migration vectors within that

corridor (Figure 5b). We do not identify any systematic differences in the performance of the two GCMs; they appear to provide equally overall accurate predictions of net sand-transport pathways

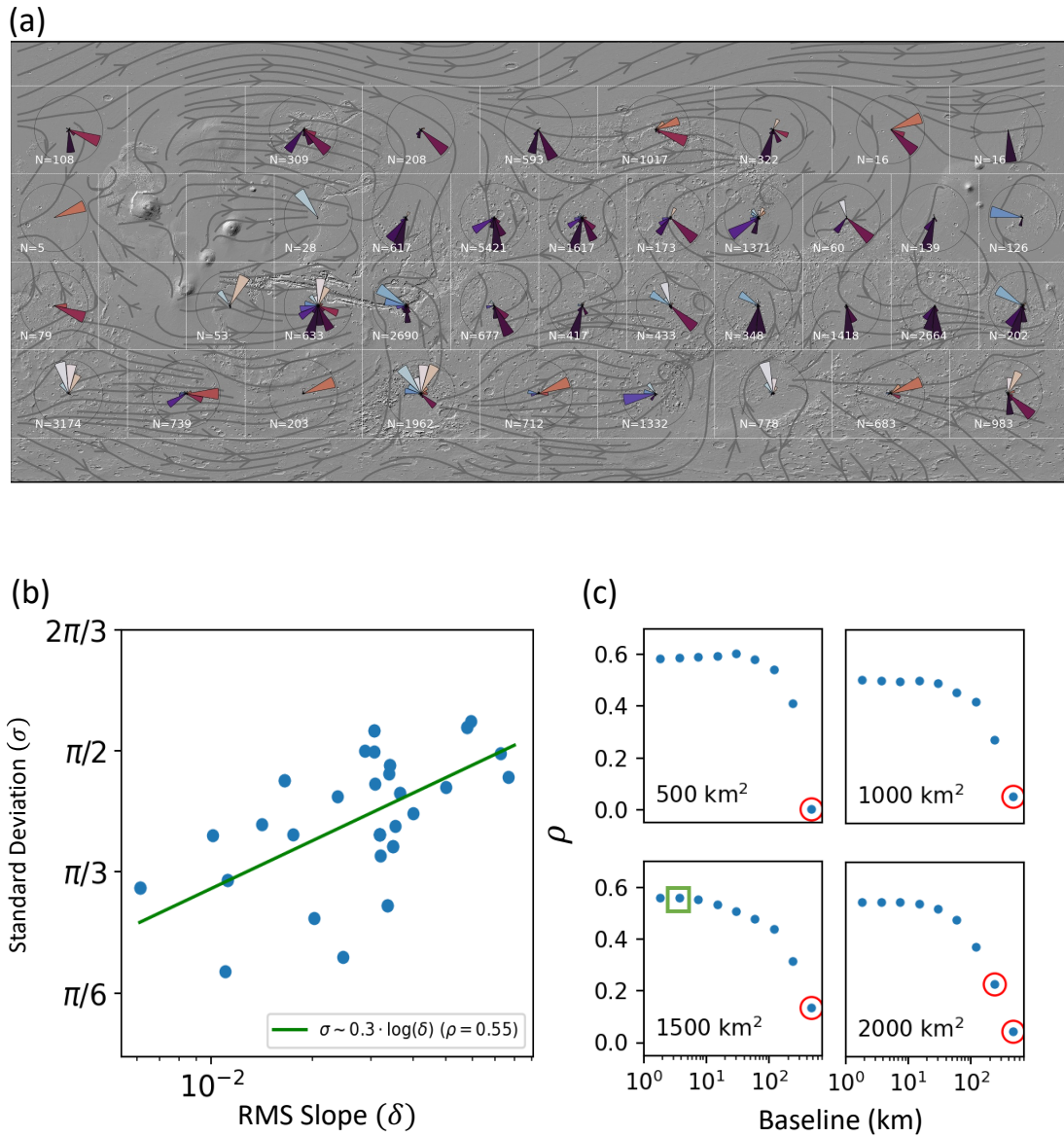


Figure 6: (a) Rose diagrams of dune-migration directions, binned in 1,500 km<sup>2</sup> equal-area bins. (b) Correlation between the RMS slope of topography,  $\delta$ , and the standard deviation of dune-migration directions,  $\sigma$ , within each spatial bin (bin area = 1,500 km<sup>2</sup>, baseline = 4 km). N values indicate the number of dunes within each bin. (c) Correlation coefficient,  $\rho$ , between  $\sigma$  and  $\delta$  as calculated for different bin sizes (labeled within each panel) and topographic baselines (x-axis). Red circles indicate non-significant ( $p > 0.05$ ; Wald test) correlations. Green square highlights the example correlation shown in (b).

## 4.2 Influence of Topography on Surface Winds

Topographic roughness from micro- to planetary scales may affect the magnitude and direction of surface winds. Specifically, deviations in wind direction from its regional trend, e.g., caused by impact craters, may result in a local misalignment between barchan migration direction and regional winds. Such deviations are notably observed in regions characterized by high topographic relief, such as Valles Marineris and the Isidis and Hellas basins, as evidenced by a larger dispersion in dune migration direction within adjacent dune fields in those regions (**Error! Reference source not found.a**).

To quantify the relationship between wind dispersion and topography, dune-migration data were binned spatially in equal-area bins. We correlated the Yamartino (angular) standard deviation of observed dune-migration directions ( $\sigma$ ) with the root mean square (RMS) slope ( $\delta$ ) derived from Mars Orbiter Laser Altimeter (MOLA; Fergason et al., 2018; Smith et al., 2001) data within each bin, resampled over a given distance, which determines the topographic baseline (the horizontal scale of the considered topographic roughness). A stronger correlation (higher correlation coefficient) between  $\sigma$  and  $\delta$  could imply that increased topographic roughness leads to a greater dispersion in dune migration directions; i.e., that the presence of topographic roughness impacts the direction of surface winds that drive dune migration. Increasing the spatial bin size increases the number of dunes within that bin, thus decreasing the statistical error in calculating  $\sigma$  and  $\delta$ , but it also leads to fewer ( $\delta, \sigma$ ) pairs from which the correlation is calculated, negatively impacting the significance of any correlations. To explore this tradeoff, we performed the analysis for wide ranges of spatial bin sizes (500–2,000 km<sup>2</sup>) and topographic baselines (2–500 km) (**Error! Reference source not found.b**).

Regardless of spatial bin size, we find a consistent correlation between  $\sigma$  and  $\delta$  for topographic baselines smaller than ~10-50 km (**Error! Reference source not found.b, c**), suggesting that at those scales, dune migration is influenced by winds induced or diverted by local topography (Chojnacki et al., 2019; Ewing & Kocurek, 2010; Hess et al., 1977; Parteli et al., 2014). The strength of the correlation between  $\sigma$  and  $\delta$  decreases with the topographic baseline, until it ceases to be statistically significant for horizontal scales > 100 km. This implies that at scales < 100 km, topography affects the regional circulation. In turn, dune migration is more affected by Mars' global circulation, which would orient dunes in the same direction and decrease  $\sigma$ . For example, dune migration within topographic depressions (such as craters) > 100 km is more likely driven by regional circulation and not, e.g., by local slope winds or winds deflected by topographic obstacles (Ewing & Kocurek, 2010; Fenton et al., 2005; Gunn et al., 2022).

Martian impact craters trap sand, which often accumulates to form dune fields or windblow deposits (Gunn et al., 2022), some of them ancient and lithified (Banham et al., 2018, 2021; Day & Catling, 2020; Day & Dorn, 2019; Grotzinger et al., 2005; Lapôtre et al., 2016, 2021; Milliken et al., 2014; Rubin et al., 2022). We find that crater depth exerts a strong control over the potential distance between the center of dune fields and the center of the crater that hosts them, such that dunes within deep craters are typically found closer to the crater center. In contrast, dunes within shallower craters (but not necessarily smaller craters) typically accumulate near the crater wall (Figure 4a). Additionally, deep craters cause dune-migration direction to deviate from the average regional migration direction (Figure 4b), as estimated by binning migration direction in the same bins as in Figure 3. For example, an increase of an order of magnitude in crater depth increases the average difference between dune-migration direction within the crater and the average regional migration direction two-folds.

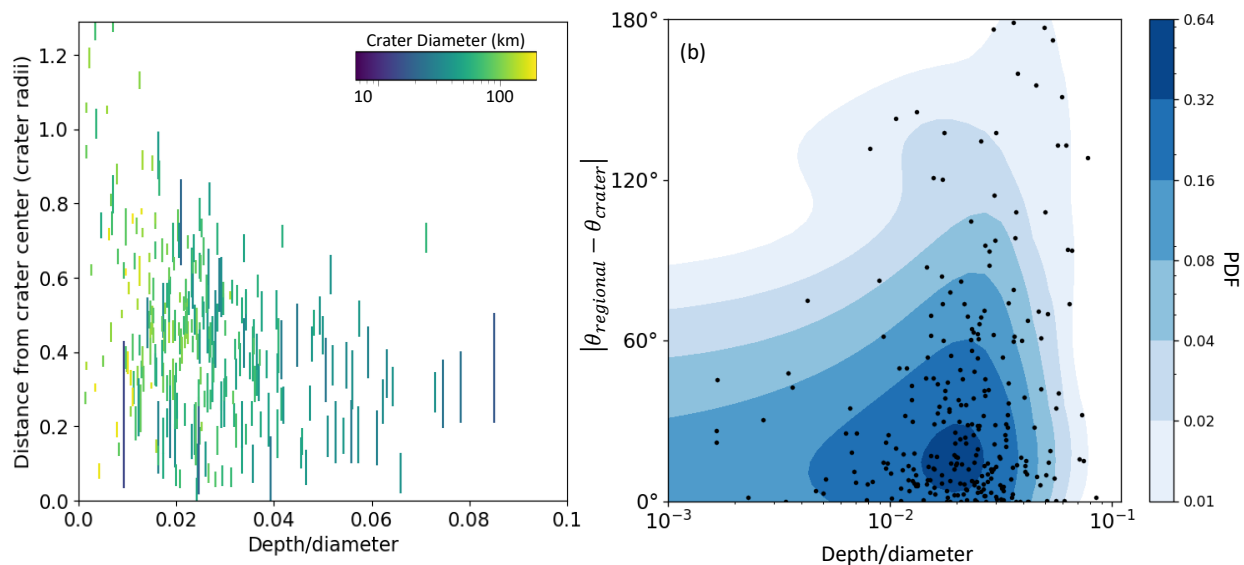


Figure 7: (a) Maximum distance between the center of mass of the dune field and the center of the crater decreases with crater depth. Error bars show the width of the dune field normalized by crater diameter. (b) Angular difference between the migration directions of intracrater dunes and dunes within the greater region outside of the crater. Migration direction of dunes within deep craters are more statistically likely to deviate from the direction of the regional migration directions (binned as in Figure 5).

## 5 Conclusion

The morphology of barchan dunes can be used to infer their migration directions as a proxy for the direction of the winds that shape them. We employed a neural network to map and outline barchan dunes globally on Mars. From dune outlines, we derived their orientation and their corresponding migration directions. In the absence of long-lived and global meteorological monitoring on Mars, our dataset provides a unique opportunity to investigate the planet's modern (Figure S4) near-surface wind circulation on a global scale.

We find that dune migration on Mars follows continuous streamlines that extend for thousands of kilometers, indicating that dune migration on the planet is mainly dictated by its global atmospheric circulation. We find that dune migration is aligned with dust-storm tracks – possibly hinting at dust lifting by saltating sand – and in good agreement with ground-based wind direction or sand-flux constraints. Misalignments between dune-migration directions and direct

measurements can in all cases be explained by winds induced by local topography. Outputs from two GCMs (LMD and MarsWRF) compare similarly well to inferred net sand-flux directions, with a few exceptions, especially in regions of high topographic relief. Notably, the GCMs do not appear to resolve an anti-cyclonic wind corridor at the base of the north polar cap.

To quantify the influence of topography on dune-migration directions, we measured the topographic roughness at different horizontal baselines. We find that the dispersion in migration directions, quantified by the angular standard deviation, increases with the topographic roughness, quantified by the RMS slope. Specifically, we find that the topographic signature of impact craters significantly influences dune formation and migration. Dune fields found within deeper craters ( $d/D > 0.01$ ) tend to be located closer to the crater center, and display larger deviations from the average regional dune-migration direction.

We hypothesize that the strong influence of topographic roughness, craters, and ice-cap valleys on surface wind directions on Mars is rooted in the planet's large swings in near-surface atmospheric stability. In stably stratified boundary layers, surface winds are isolated from the geostrophic winds aloft and as a result, tend to be slower and guided by topographic features (Gadal et al., 2022). In contrast, surface winds in a convective boundary layer tend to be faster and have an outsized influence on sand transport (Gunn et al., 2021). Katabatic winds down the ice-cap valleys and some crater walls are expected to be strong on Mars due to such large diurnal variations in boundary-layer stability. Critically, these processes are challenging for GCMs to resolve due to parameterizations of non-equilibrium stability effects in the boundary layer, as well as spatial resolution. Our results are thus compelling evidence that discrepancies between observation and simulation manifest through the interaction of topography and the stability of the near-surface atmosphere on Mars. Therefore, caution needs to be applied when interpreting paleo-wind directions on Mars from ancient aeolian sandstones. As sedimentary sinks, many impact craters on Mars have preserved an aeolian sedimentary record. The strong influence of crater topography on sediment accumulation and wind direction is likely to be reflected in the stratigraphy of craters with diameters  $< 100$  km, and those strata may neither provide a direct record of regional winds nor be reproducible by current GCMs.

### Acknowledgments

This work was supported in part by NASA grants 80NSSC20K0145 to MGAL and 80NSSC21K1090 to RCE.

### Data Availability

Data used in this study can be accessed through this link:

[https://figshare.com/articles/dataset/dunes\\_migration\\_csv/21755843](https://figshare.com/articles/dataset/dunes_migration_csv/21755843)

### Code Availability

Code used to process the data is available here: <https://doi.org/10.5281/zenodo.7305150>.

## References

- Ayoub, F., Avouac, J.-P., Newman, C. E., Richardson, M. I., Lucas, A., Leprince, S., & Bridges, N. T. (2014). Threshold for sand mobility on Mars calibrated from seasonal variations of sand flux. *Nature Communications*, 5(1), 1–8.

- Baker, M. M., Newman, C. E., Lapotre, M. G. A., Sullivan, R., Bridges, N. T., & Lewis, K. W. (2018). Coarse sediment transport in the modern Martian environment. *JGR: Planets*, *123*(6), 1380–1394.
- Baker, M. M., Lapôtre, M. G. A., Minitti, M. E., Newman, C. E., Sullivan, R., Weitz, C. M., et al. (2018). The Bagnold Dunes in southern summer: Active sediment transport on Mars observed by the Curiosity rover. *Geophysical Research Letters*, *45*(17), 8853–8863.
- Baker, M. M., Newman, C. E., Sullivan, R., Minitti, M. E., Edgett, K. S., Fey, D., et al. (2022). Diurnal variability in aeolian sediment transport at Gale crater, Mars. *JGR: Planets*, *127*(2), e2020JE006734.
- Banfield, D., Spiga, A., Newman, C., Forget, F., Lemmon, M., Lorenz, R., et al. (2020). The atmosphere of Mars as observed by InSight. *Nature Geoscience*, *13*(3), 190–198.
- Banham, S. G., Gupta, S., Rubin, D. M., Watkins, J. A., Sumner, D. Y., Edgett, K. S., et al. (2018). Ancient Martian aeolian processes and palaeomorphology reconstructed from the Stimson formation on the lower slope of Aeolis Mons, Gale crater, Mars. *Sedimentology*, *65*(4), 993–1042.
- Banham, S. G., Gupta, S., Rubin, D. M., Edgett, K. S., Barnes, R., Van Beek, J., et al. (2021). A rock record of complex aeolian bedforms in a Hesperian desert landscape: the Stimson formation as exposed in the Murray buttes, Gale crater, Mars. *JGR: Planets*, *126*(4), e2020JE006554.
- Battalio, M., & Wang, H. (2021). The Mars Dust Activity Database (MDAD): A comprehensive statistical study of dust storm sequences. *Icarus*, *354*, 114059.
- Bourke, M. C., & Goudie, A. S. (2009). Varieties of barchan form in the Namib Desert and on Mars. *Aeolian Research*, *1*(1–2), 45–54. <https://doi.org/10.1016/j.aeolia.2009.05.002>
- Breed, C. S., Grolier, M. J., & McCauley, J. F. (1979). Morphology and distribution of common ‘sand’ dunes on Mars: Comparison with the Earth. *Journal of Geophysical Research: Solid Earth*, *84*(B14), 8183–8204.
- Bridges, N. T., Bourke, M. C., Geissler, P. E., Banks, M. E., Colon, C., Diniega, S., et al. (2012). Planet-wide sand motion on Mars. *Geology*, *40*(1), 31–34.
- Bridges, N. T., Sullivan, R., Newman, C. E., Navarro, S., Van Beek, J., Ewing, R. C., et al. (2017). Martian aeolian activity at the Bagnold Dunes, Gale Crater: The view from the surface and orbit. *JGR: Planets*, *122*(10), 2077–2110.
- Cantor, B. A., James, P. B., Caplinger, M., & Wolff, M. J. (2001). Martian dust storms: 1999 Mars orbiter camera observations. *Journal of Geophysical Research: Planets*, *106*(E10), 23653–23687.
- Chojnacki, M., Banks, M. E., Fenton, L. K., & Urso, A. C. (2019). Boundary condition controls on the high-sand-flux regions of Mars. *Geology*, *47*(5), 427–430.
- Day, M., & Catling, D. C. (2020). Potential aeolian deposition of intra-crater layering: A case study of Henry crater, Mars. *Bulletin*, *132*(3–4), 608–616.
- Day, M., & Dorn, T. (2019). Wind in Jezero crater, Mars. *Geophysical Research Letters*, *46*(6), 3099–3107.

- Dickson, J. L., Kerber, L. A., Fassett, C. I., & Ehlmann, B. L. (2018). A global, blended CTX mosaic of Mars with vectorized seam mapping: A new mosaicking pipeline using principles of non-destructive image editing. In *LPSC* (Vol. 49, pp. 1–2).
- Diniega, S., Bramson, A. M., Buratti, B., Buhler, P., Burr, D. M., Chojnacki, M., et al. (2021). Modern Mars' geomorphological activity, driven by wind, frost, and gravity. *Geomorphology*, *380*, 107627.
- Ewing, R. C., & Kocurek, G. A. (2010). Aeolian dune interactions and dune-field pattern formation: White Sands Dune Field, New Mexico. *Sedimentology*, *57*(5), 1199–1219.
- Ewing, R. C., Lapôtre, M. G. A., Lewis, K. W., Day, M., Stein, N., Rubin, D. M., et al. (2017). Sedimentary processes of the Bagnold Dunes: Implications for the eolian rock record of Mars. *Journal of Geophysical Research: Planets*, *122*(12), 2544–2573.
- Fenton, L. K. (2020). Updating the global inventory of dune fields on Mars and identification of many small dune fields. *Icarus*, *352*, 114018.
- Fenton, L. K., & Hayward, R. K. (2010). Southern high latitude dune fields on Mars: Morphology, aeolian inactivity, and climate change. *Geomorphology*, *121*(1–2), 98–121.
- Fenton, L. K., Toigo, A. D., & Richardson, M. I. (2005). Aeolian processes in Proctor Crater on Mars: Mesoscale modeling of dune-forming winds. *Journal of Geophysical Research: Planets*, *110*(E6).
- Ferguson, R. L., Hare, T. M., & Laura, J. (2018). HRSC and MOLA blended digital elevation model at 200m v2, astrogeology PDS annex. *US Geological Survey*.
- Forget, F., Hourdin, F., Fournier, R., Hourdin, C., Talagrand, O., Collins, M., et al. (1999). Improved general circulation models of the Martian atmosphere from the surface to above 80 km. *Journal of Geophysical Research: Planets*, *104*(E10), 24155–24175.
- Gadal, C., Delorme, P., Narteau, C., Wiggs, G. F. S., Baddock, M., Nield, J. M., & Claudin, P. (2022). Local wind regime induced by giant linear dunes: comparison of ERA5-land reanalysis with surface measurements. *Boundary-Layer Meteorology*, *185*(3), 309–332.
- Gao, X., Narteau, C., Rozier, O., & Du Pont, S. C. (2015). Phase diagrams of dune shape and orientation depending on sand availability. *Scientific Reports*, *5*(1), 1–12.
- Greeley, R. (2002). Saltation impact as a means for raising dust on Mars. *Planetary and Space Science*, *50*(2), 151–155.
- Greeley, R., White, B. R., Pollack, J. B., Iversen, J. D., & Leach, R. N. (1981). Dust storms on Mars: Considerations and simulations. *Spec. Pap. Geol. Soc. Am.*, *186*, 101–121.
- Grotzinger, J. P., Arvidson, R. E., Bell III, J. F., Calvin, W., Clark, B. C., Fike, D. A., et al. (2005). Stratigraphy and sedimentology of a dry to wet eolian depositional system, Burns formation, Meridiani Planum, Mars. *Earth and Planetary Science Letters*, *240*(1), 11–72.
- Gunn, A., Wanker, M., Lancaster, N., Edmonds, D. A., Ewing, R. C., & Jerolmack, D. J. (2021). Circadian rhythm of dune-field activity. *Geophysical Research Letters*, *48*(5), e2020GL090924.
- Gunn, A., Rubanenko, L., & Lapôtre, M. G. A. (2022). Accumulation of windblown sand in impact craters on Mars. *Geology*.

- Hayward, R. K., Mullins, K. F., Fenton, L. K., Hare, T. M., Titus, T. N., Bourke, M. C., et al. (2007). Mars global digital dune database and initial science results. *Journal of Geophysical Research: Planets*, 112(E11).
- Hayward, R. K., Fenton, L. K., Titus, T. N., Colaprete, A., & Christensen, P. R. (2012). Mars global digital dune database: MC-30. *US Geological Survey Open-File Report*, 1259.
- He, K., Gkioxari, G., Dollár, P., & Girshick, R. (2017). Mask R-CNN. *IEEE ICCV*.
- Hess, S. L., Henry, R. M., Leovy, C. B., Ryan, J. A., & Tillman, J. E. (1977). Meteorological results from the surface of Mars: Viking 1 and 2. *JGR*, 82(28), 4559–4574.
- Kite, E. S. (2019). Geologic constraints on early Mars climate. *Space Science Reviews*, 215(1), 1–47.
- Lancaster, N., & Greeley, R. (1990). Sediment volume in the north polar sand seas of Mars. *Journal of Geophysical Research: Solid Earth*, 95(B7), 10921–10927.
- Lapôtre, M. G. A., & Rampe, E. B. (2018). Curiosity’s investigation of the Bagnold Dunes, Gale crater: Overview of the two-phase scientific campaign and introduction to the special collection. *Geophysical Research Letters*, 45(19), 10–200.
- Lapôtre, M. G. A., Ewing, R. C., Lamb, M. P., Fischer, W. W., Grotzinger, J. P., Rubin, D. M., et al. (2016). Large wind ripples on Mars: A record of atmospheric evolution. *Science*, 353(6294), 55–58.
- Lapôtre, M. G. A., O’Rourke, J. G., Schaefer, L. K., Siebach, K. L., Spalding, C., Tikoo, S. M., & Wordsworth, R. D. (2020). Probing space to understand Earth. *Nature Reviews Earth & Environment*, 1(3), 170–181.
- Lapôtre, M. G. A., Ewing, R. C., & Lamb, M. P. (2021). An evolving understanding of enigmatic large ripples on Mars. *Journal of Geophysical Research: Planets*, 126(2), e2020JE006729.
- Levine, J. S., Kerschmann, R. L., & Winterhalter, D. (2018). *Dust in the atmosphere of Mars and its impact on human exploration*. Cambridge Scholars Publishing.
- Malin, M. C., Bell, J. F., Cantor, B. A., Caplinger, M. A., Calvin, W. M., Clancy, R. T., et al. (2007). Context camera investigation on board the Mars Reconnaissance Orbiter. *Journal of Geophysical Research: Planets*, 112(E5).
- Martin, R. L., & Kok, J. F. (2017). Wind-invariant saltation heights imply linear scaling of aeolian saltation flux with shear stress. *Science Advances*, 3(6), e1602569.
- Milliken, R. E., Ewing, R. C., Fischer, W. W., & Hurowitz, J. (2014). Wind-blown sandstones cemented by sulfate and clay minerals in Gale Crater, Mars. *Geophysical Research Letters*, 41(4), 1149–1154.
- Millour, E., Forget, F., Spiga, A., Vals, M., Zakharov, V., & Montabone, L. (2018). Mars climate database. In *From Mars Express to ExoMars, 27-28 February 2018, Madrid, Spain*.
- Montabone, L., & Forget, F. (2018). On forecasting dust storms on Mars. 48th International Conference on Environmental Systems.
- Newman, C. E., Lewis, S. R., Read, P. L., & Forget, F. (2002). Modeling the Martian dust cycle, 1. Representations of dust transport processes. *JGR: Planets*, 107(E12), 1–6.

- Parteli, E. J. R., Durán, O., Bourke, M. C., Tsoar, H., Pöschel, T., & Herrmann, H. (2014). Origins of barchan dune asymmetry: Insights from numerical simulations. *Aeolian Research*, *12*, 121–133.
- Pollack, J. B., Haberle, R., Greeley, R., & Iversen, J. (1976). Estimates of the wind speeds required for particle motion on Mars. *Icarus*, *29*(3), 395–417.
- Richardson, M. I., Toigo, A. D., & Newman, C. E. (2007). PlanetWRF: A general purpose, local to global numerical model for planetary atmospheric and climate dynamics. *JGR: Planets*, *112*(E9).
- Rubanenko, L., Pérez-López, S., Schull, J., & Lapôtre, M. G. A. (2021). Automatic Detection and Segmentation of Barchan Dunes on Mars and Earth Using a Convolutional Neural Network. *IEEE Journal of Selected Topics in Applied Earth Observations and Remote Sensing*, *14*, 9364–9371.
- Rubanenko, L., Lapotre, M. G. A., Ewing, R. C., Fenton, L. K., & Gunn, A. (2022). A distinct ripple-formation regime on Mars revealed by the morphometrics of barchan dunes. *Nature Communications*.
- Rubin, D. M., Lapôtre, M. G. A., Stevens, A. W., Lamb, M. P., Fedo, C. M., Grotzinger, J. P., et al. (2022). Ancient Winds, Waves, and Atmosphere in Gale Crater, Mars, Inferred From Sedimentary Structures and Wave Modeling. *Journal of Geophysical Research: Planets*, e2021JE007162.
- Smith, D. E., Zuber, M. T., Frey, H. V., Garvin, J. B., Head, J. W., Muhleman, D. O., et al. (2001). Mars Orbiter Laser Altimeter: Experiment summary after the first year of global mapping of Mars. *Journal of Geophysical Research: Planets*, *106*(E10), 23689–23722.
- Spiga, A., & Smith, I. (2018). Katabatic jumps in the Martian northern polar regions. *Icarus*, *308*, 197–208.
- Tsoar, H., & Parteli, E. J. R. (2016). Bidirectional winds, barchan dune asymmetry and formation of seif dunes from barchans: a discussion. *Environmental Earth Sciences*, *75*(18), 1–10.
- Tsoar, H., Greeley, R., & Peterfreund, A. R. (1979). Mars: The north polar sand sea and related wind patterns. *Journal of Geophysical Research: Solid Earth*, *84*(B14), 8167–8180.
- Ward, A. W., Doyle, K. B., Helm, P. J., Weisman, M. K., & Witbeck, N. E. (1985). Global map of eolian features on Mars. *Journal of Geophysical Research: Solid Earth*, *90*(B2), 2038–2056.
- Werner, B. T. (1990). A steady-state model of wind-blown sand transport. *The Journal of Geology*, *98*(1), 1–17.
- Wordsworth, R. D. (2016). The climate of early Mars. *Annual Review of Earth and Planetary Sciences*, *44*, 381–408.
- Zuber, M. T. (2003). Learning to think like martians. *Science*, *302*(5651), 1694–1695.

**Supplementary Information for “Global Surface Winds and Aeolian Sediment Pathways on Mars from the Morphology of Barchan Dunes”**

**L. Rubanenko<sup>1,2</sup>, A. Gunn<sup>1,3</sup>, S. Pérez-López<sup>1</sup>, L.K. Fenton<sup>4</sup>, R.C. Ewing<sup>5</sup>, Alejandro Soto<sup>6</sup> and M.G.A Lapôtre<sup>1</sup>**

<sup>1</sup> Department of Earth & Planetary Sciences, Stanford University, Stanford, California, USA.

<sup>2</sup> Civil and Environmental Engineering, Technion, Haifa, Israel.

<sup>3</sup> School of Earth, Atmosphere & Environment, Monash University, Clayton, Australia.

<sup>4</sup> Carl Sagan Center, SETI Institute, Mountain View, California, USA.

<sup>5</sup> Department of Geology & Geophysics, Texas A&M, College Station, Texas, USA.

<sup>6</sup> Southwest research Institute, Boulder, Colorado, USA.

**1. Filtering Process of Barchan Dune’s Outlined by the Neural Network**

To increase the robustness of our compilation, we filtered our dataset as follows:

(1) Between 70°S-70°N, we only used images of areas previously mapped as dune fields (Fenton, 2020; Hayward et al., 2012). This was done to save computation time – since our goal is not to detect new barchan dunes on Mars but to characterize migration directions of dunes on Mars on a global scale.

(2) Because barchans tend to occur in fields rather than as solitary landforms, we discarded images (800x800 pixels; 4x4 km) containing less than three objects to remove potentially spurious detections.

(3) Upon manually inspecting our results, we found that the model misclassified some dark sublimation-driven features at southern polar latitudes, such as Dalmatian spots and spiders (Zuber, 2003), as barchans. Consequently, we elected to discard dunes in latitudes poleward of 70°S.

(4) By removing dunes with detection-confidence levels outputted by the detection algorithm lower than 70%, and dunes with convexity defects smaller than 2.5% of total dune length (length + mean horn length). The latter step removed many isolated objects erroneously identified as dunes, but also isolated dome dunes, which are excluded from this study. Our choice of 70% confidence is based on trial and error and visual inspection of the detected objects.

**2. Validating Methodology with Manual and In-Situ Measurements on Earth**

We validate our approach of determining the dominant wind direction by comparing the migration direction of terrestrial dunes computed from images of terrestrial dunes with independent, direct measurements of sand flux (Figure S1). The average migration direction of all the dunes in the scene agrees with the sand flux measured in the same area.

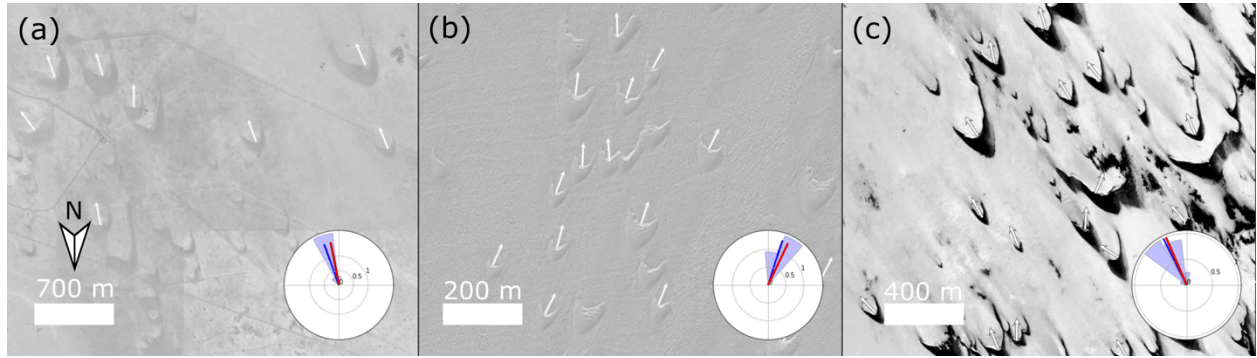


**Figure S1:** Average barchan migration directions computed from images (blue dial) and direct measurements of sand flux (red dial) in (a) Qatar ( $25.04^{\circ}\text{N}$ ,  $51.40^{\circ}\text{E}$ ): sand flux measured 30 km east of the dune field (b) Sahara ( $27.7^{\circ}\text{N}$ ,  $-12.98^{\circ}\text{E}$ ): sand flux measured 26 km west from the dune field (Elbelrhiti et al., 2008) (c) Chad ( $16.68^{\circ}\text{N}$ ,  $17.88^{\circ}\text{E}$ ): sand flux measured 50 km east of the dune field (Baird et al., 2019).

### 3. Wind-Direction Constraints on Mars from Ground Observations

To further compare with our derived map of global barchan-migration direction (Figure 2), we compiled in-situ measurements wind directions or available proxies on Mars (yellow arrows in Figure 2a):

- (1) Viking Lander 1: average 20-sol composite values of wind measurements taken at local lander times 0240, 0701, and 1122 (Hess et al., 1977)
- (2) Mars Pathfinder: average orientation of bright wind streaks imaged by the lander and rover (Greeley et al., 1999).
- (3) Spirit & Opportunity: wind tail, facet, and groove orientations images by Pancam, Navcam, and Hazcam (Greeley et al., 2008; Sullivan et al., 2005).
- (4) Phoenix: anemometer readings collected over the course of 150 sols, weighted by sand flux (Holstein-Rathlou et al., 2010)
- (5) Curiosity: ripple migration vectors measured by Mastcam and Mars Descent Imager (MARDI) (Baker et al., 2018; Viúdez-Moreiras et al., 2019)
- (6) Insight: TWINS (temperature and wind for Insight) readings were used to compute the wind direction, weighted by wind speeds, computed on three distinct sols ( $L_s = 13^{\circ}$ ,  $307^{\circ}$  and  $324^{\circ}$ ) (Banfield et al., 2020).
- (7) Jezero: wind streaks orientations near the Perseverance landing site, derived from HiRISE images (Day & Dorn, 2019; Newman et al., 2022).

### 4. Global Sand Flux Predictions by the MarsWRF Climate Model

In addition to predictions of global sand flux on Mars by the LMD MCD (Figure 2), we compare our derived migration directions with predictions by the Mars Weather and Research Forecasting (MarsWRF) global general circulation model (Richardson et al., 2007; Figure S2). We use the same simulation setup as Rivera-Valentín et al. (2020) and Chevrier et al. (2020). The model was run with a non-prescribed dust scheme, a  $\text{CO}_2$  cycle, and a water cycle that included radiatively active water and dust (Lee et al., 2018).

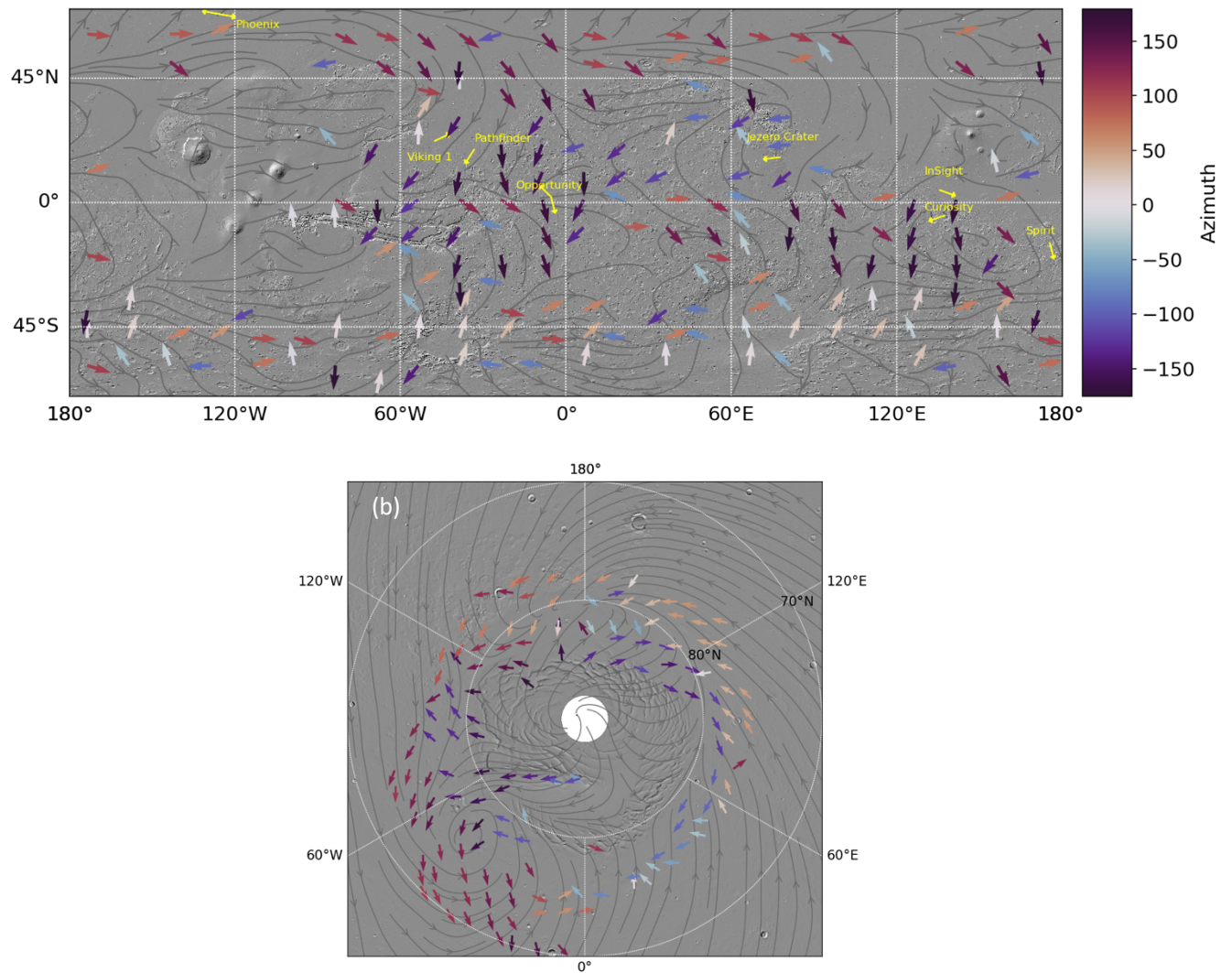


**Figure S2:** MarsWRF sand flux predictions (gray streamlines) and dune-migration directions (arrows) on Mars. (a) 70S °–70°N. (b) >70°N. Yellow arrows with labels indicate local estimates of wind or sand flux direction from landed spacecraft.

## 5. Comparing Sand Flux Predictions by MarsWRF and LMD GCMs

To compare sand flux predictions by the two GCMs (Figure S3), we compute the angular difference between their predictions and the measured migration direction. We find both models provide equally good predictions of the migration direction of barchan dunes on Mars. The source of the deviation can be mostly explained by local slopes affecting the global or regional circulation (see discussion in main text).

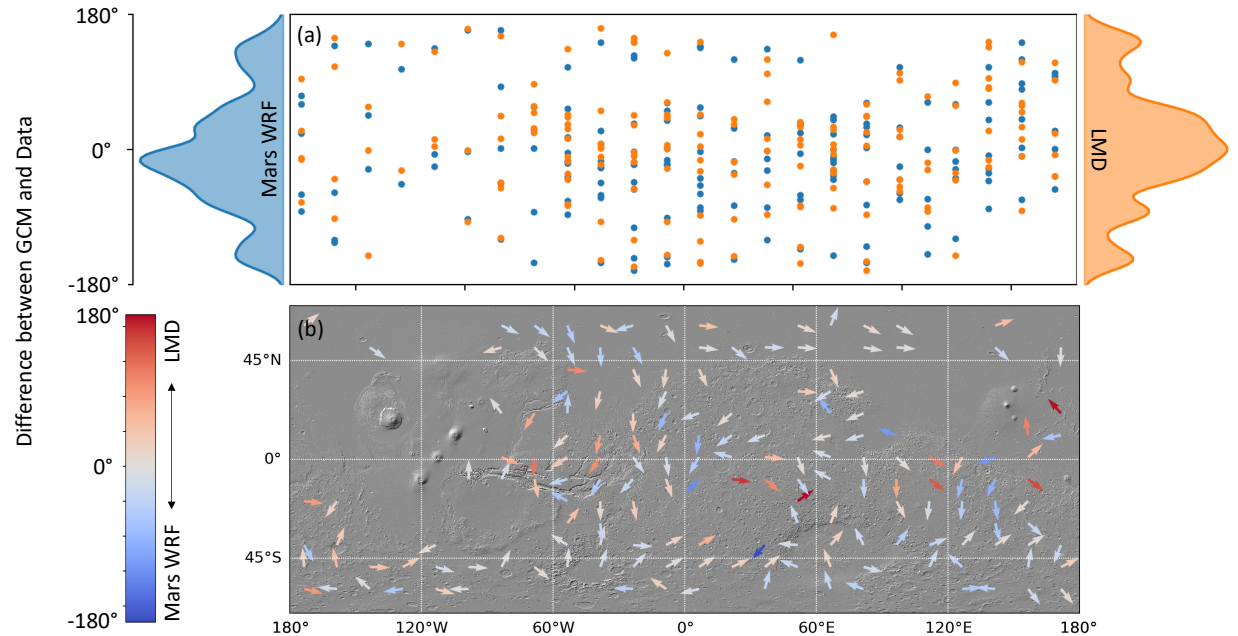


**Figure S3:** Comparison between the predictions of the two GCMs (LMD and MarsWRF). (a) Angular difference between GCM-predicted sand flux and dune-migration directions, sorted by longitude (horizontal axis). Marginal histograms show the performance of each model. (b) Migration directions of barchan dunes across Mars. Colors indicate the difference in dune-data/model discrepancies between the two models. Blue arrows reflect locations where MarsWRF is in better agreement with barchan-dune migration directions, whereas red arrows indicate locations where the LMD model performs better.

## 6. Bedform reconstitution timescale

To assess the duration over which barchan-dune morphology and orientation integrate over on Mars, we calculated the bedform reconstitution timescale (e.g., Bagnold, 1942) from compiled dune morphometrics. The reconstitution timescale is the time it takes for a barchan dune to migrate one wavelength and is a good approximation for the time it would take to orient itself with the net above-threshold wind direction. It is calculated as  $T_R = L/c$ , where dune length  $L$  (m) is found as defined in Rubanenko et al., 2022 and migration rate,  $c$  (m/s), is the speed the barchan slipface advances in the orientation direction.

Predicted migration rate,  $c_p$ , is calculated by pairing the LMD GCM predicted sand flux and dune geometry height,  $H$ , from Rubanenko et al., 2022, then calibrated to measured slipface advancing rates measured by Bridges et al. (2012) and Chojnacki et al. (2019) at Nili Patera. Slipface migration,  $c_p$ , is defined as  $c_p = q/(H\phi\rho_s)$ , where  $q$  (kg/m/s) is the sediment flux,  $\phi$  is the packing fraction, and  $\rho_s$  (kg/m<sup>3</sup>) is the sediment density. We assume typical global values for  $\phi = 0.7$  and  $\rho_s = 3000$  kg/m<sup>3</sup>.

Sediment flux,  $q$ , is estimated in three steps. First, the net saturated flux vector from the LMD GCM,  $\vec{q}_s$  (kg/m/s), is calculated from the 10-m wind vectors using the Martin & Kok (2017) flux law, as described elsewhere in the text. Second, this flux vector is projected onto the dune migration direction,  $\theta_d$ , such that the flux in the saturated flux in dune direction,  $q_{s,d} = |\vec{q}_s| |\cos(\angle \vec{q}_s - \theta_d)|$ . Third, the saturated flux in the dune direction is scaled to the true flux the barchan experiences,  $q$ , which is the average stoss flux. The average stoss flux is the average of the flux at the toe (which is zero since we are only considering isolated barchans) and the flux at the brink,  $q_b$ , which is higher than the saturated flux due to the wind speed-up effect over the positive stoss slope. Thus,  $q = q_b/2$ . The brink flux is calculated as  $q_b = q_{s,d}(1 + \beta s)$ , where  $\beta$  is a dimensionless speed-up factor of  $\sim 9.44$  for dunes (Gunn, 2022), and  $s$  is the stoss slope  $s = H/(L - H/\tan \theta_{sf})$ , where  $\theta_{sf} = 30^\circ$  is the slipface angle.

Predictions of dune migration rate,  $c$ , made as described above from LMD GCM outputs, chosen flux law, and barchan geometries are smaller than observed martian dune migration rates measured using repeat HiRISE images by Chojnacki et al. (2019) and Bridges et al. (2012). This discrepancy is to be expected for a variety of reasons, including potential misrepresentation of near-surface winds in the GCM as demonstrated by other results in the paper, and the fact that flux laws have not been directly calibrated to saltation on Mars. We do believe, however, that despite the error in absolute values in migration speeds, the spatial pattern in relative migration speeds is relatively robust (Fig. S4a). This is because while the Earth-calibrated prefactor from the Martin & Kok (2014) flux law may not hold on Mars, the exponent in the flux relationship should be more reliable. As a result, we can empirically calibrate  $c$  as  $c = c_p c_{NP,m}/c_{NP,p}$ , where  $c_{NP,m}$  is the mean of measured dune migration speeds,  $c_m$ , at Nili Patera ( $c_{NP,m} \approx 0.769$  m/Earth year or m/EY as estimated by Chojnacki et al., 2019, or 0.562 m/EY as estimated by Bridges et al., 2012). This recalibration still does not include the effect of surface volatiles, where seasonal frost away from the equator may affect the calculated migration rates, and hence,  $T_R$ .

Finally, the probability distribution of calculated  $T_R$  values are given as  $T_R = L/c$  in Fig. S4b. The mode of this distribution is approximately 100 Mars years (MY), with a range from 10 to  $10^4$  MY. In comparison Mars' obliquity, eccentricity, and precession display periods of  $\sim 64 \times 10^3$ ,  $50 \times 10^3$ , and  $\sim 27 \times 10^3$  MY, with additional periods that exceed  $10^6$  EY (Schorghofer, 2008). Such short reconstitution timescales confirm that derived dune migration directions reflect the modern wind circulation of Mars rather than past conditions (Fenton & Richardson, 2001). We emphasize again that these short reconstitution timescales only reflect those of isolated barchan dunes; larger dunes would have longer reconstitution timescales, and in turn, may record information about recent atmospheric change on Mars (Ewing et al., 2010).

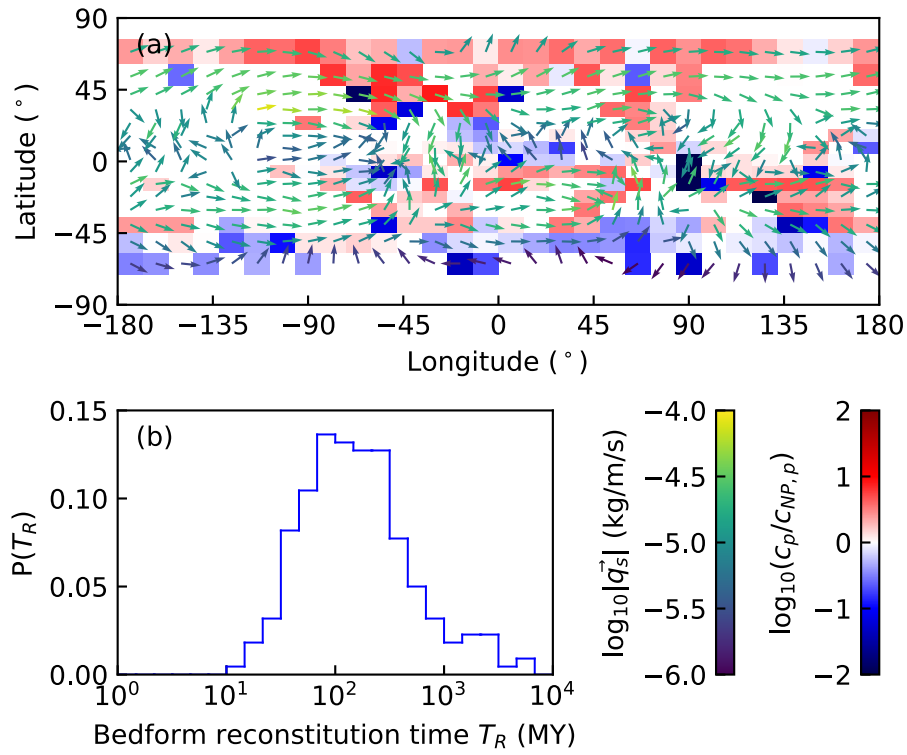


**Figure S4.** (a) Map of Mars colored by the logarithm of the predicted dune migration speeds,  $c_p$  (m/s), normalised by the predicted dune migration speed at Nili Patera,  $c_{NP,p}$  (m/s), overlaid by the saturated flux vector directions colored by the logarithm of the flux vector magnitudes predicted by the LMD GCM. (b) The global probability distribution of the predicted bedform reconstitution times,  $T_R$  (MY).

## **References:**

- Bagnold, R. A. (1942). *The physics of blown sand and desert dunes*. New York, W. Morrow & company.
- Baird, T., Bristow, C. S., & Vermeesch, P. (2019). Measuring sand dune migration rates with COSI-Corr and landsat: Opportunities and challenges. *Remote Sensing*, *11*(20), 2423.
- Baker, M. M., Lapôte, M. G. A., Minitti, M. E., Newman, C. E., Sullivan, R., Weitz, C. M., et al. (2018). The Bagnold Dunes in southern summer: Active sediment transport on Mars observed by the Curiosity rover. *Geophysical Research Letters*, *45*(17), 8853–8863.
- Banfield, D., Spiga, A., Newman, C., Forget, F., Lemmon, M., Lorenz, R., et al. (2020). The atmosphere of Mars as observed by InSight. *Nature Geoscience*, *13*(3), 190–198.
- Bridges, N. T., Bourke, M. C., Geissler, P. E., Banks, M. E., Colon, C., Diniega, S., et al. (2012). Planet-wide sand motion on Mars. *Geology*, *40*(1), 31–34.
- Chevrier, V. F., Rivera-Valentín, E. G., Soto, A., & Altheide, T. S. (2020). Global temporal and geographic stability of brines on present-day Mars. *The Planetary Science Journal*, *1*(3), 64.
- Chojnacki, M., Banks, M. E., Fenton, L. K., & Urso, A. C. (2019). Boundary condition controls on the high-sand-flux regions of Mars. *Geology*, *47*(5), 427–430.
- Day, M., & Dorn, T. (2019). Wind in Jezero crater, Mars. *Geophysical Research Letters*, *46*(6), 3099–3107.
- Elbelrhiti, H., Andreotti, B., & Claudin, P. (2008). Barchan dune corridors: field characterization and investigation of control parameters. *JGR: Earth Surface*, *113*(F2).
- Ewing, R. C., Peyret, A. B., Kocurek, G., & Bourke, M. (2010). Dune field pattern formation and recent transporting winds in the Olympia Undae Dune Field, north polar region of Mars. *Journal of Geophysical Research: Planets*, *115*(E8).
- Fenton, L. K. (2020). Updating the global inventory of dune fields on Mars and identification of many small dune fields. *Icarus*, *352*, 114018.
- Fenton, L. K., & Richardson, M. I. (2001). Martian surface winds: Insensitivity to orbital changes and implications for aeolian processes. *Journal of Geophysical Research: Planets*, *106*(E12), 32885–32902.
- Greeley, R., Kraft, M., Sullivan, R., Wilson, G., Bridges, N., Herkenhoff, K., et al. (1999). Aeolian features and processes at the Mars Pathfinder landing site. *JGR: Planets*, *104*(E4), 8573–8584.
- Greeley, R., Whelley, P. L., Neakrase, L. D. V., Arvidson, R. E., Bridges, N. T., Cabrol, N. A., et al. (2008). Columbia Hills, Mars: Aeolian features seen from the ground and orbit. *JGR: Planets*, *113*(E6).
- Hayward, R. K., Fenton, L. K., Titus, T. N., Colaprete, A., & Christensen, P. R. (2012). Mars global digital dune database: MC-30. *US Geological Survey Open-File Report*, 1259.
- Hess, S. L., Henry, R. M., Leovy, C. B., Ryan, J. A., & Tillman, J. E. (1977). Meteorological results from the surface of Mars: Viking 1 and 2. *JGR*, *82*(28), 4559–4574.
- Holstein-Rathlou, C., Gunnlaugsson, H. P., Merrison, J. P., Bean, K. M., Cantor, B. A., Davis, J. A., et al.

- (2010). Winds at the Phoenix landing site. *JGR: Planets*, 115(E5).
- Lee, C., Richardson, M. I., Newman, C. E., & Mischna, M. A. (2018). The sensitivity of solsticial pauses to atmospheric ice and dust in the MarsWRF General Circulation Model. *Icarus*, 311, 23–34.
- Martin, R. L., & Kok, J. F. (2017). Wind-invariant saltation heights imply linear scaling of aeolian saltation flux with shear stress. *Science Advances*, 3(6), e1602569.
- Newman, C. E., Hueso, R., Lemmon, M. T., Munguira, A., Vicente-Retortillo, Á., Apestigue, V., et al. (2022). The dynamic atmospheric and aeolian environment of Jezero crater, Mars. *Science Advances*, 8(21), eabn3783.
- Richardson, M. I., Toigo, A. D., & Newman, C. E. (2007). PlanetWRF: A general purpose, local to global numerical model for planetary atmospheric and climate dynamics. *JGR: Planets*, 112(E9).
- Rivera-Valentín, E. G., Chevrier, V. F., Soto, A., & Martínez, G. (2020). Distribution and habitability of (meta) stable brines on present-day Mars. *Nature Astronomy*, 4(8), 756–761.
- Rubanenko, L., Lapotre, M. G. A., Ewing, R. C., Fenton, L. K., & Gunn, A. (2022). A distinct ripple-formation regime on Mars revealed by the morphometrics of barchan dunes. *Nature Communications*.
- Schorghofer, N. (2008). Temperature response of Mars to Milankovitch cycles. *Geophysical Research Letters*, 35(18).
- Sullivan, R., Banfield, D., Bell, J. F., Calvin, W., Fike, D., Golombek, M., et al. (2005). Aeolian processes at the Mars exploration rover Meridiani Planum landing site. *Nature*, 436(7047), 58–61.
- Viúdez-Moreiras, D., Gómez-Elvira, J., Newman, C. E., Navarro, S., Marin, M., Torres, J., & De La Torre-Juárez, M. (2019). Gale surface wind characterization based on the Mars Science Laboratory REMS dataset. Part I: Wind retrieval and Gale's wind speeds and directions. *Icarus*, 319, 909–925.
- Zuber, M. T. (2003). Learning to think like martians. *Science*, 302(5651), 1694–1695.